Materials Science & Engineering R 152 (2023) 100714

Contents lists available at ScienceDirect

Materials Science & Engineering R

journal homepage: www.elsevier.com/locate/mser

Emerging applications of metal-organic frameworks and derivatives in solar cells: Recent advances and challenges

Binling Chen [a,b], Zhuxian Yang [a], Quanli Jia [c], Richard J. Ball [d], Yanqiu Zhu [a], Yongde Xia [a,*]

[a] College of Engineering, Mathematics and Physical Sciences, University of Exeter, Exeter EX4 4QF, United Kingdom
[b] School of Mechanical Engineering, Beijing Institute of Technology, Beijing 100081, PR China
[c] Henan Key Laboratory of High Temperature Functional Ceramics, Zhengzhou University, Zhengzhou 450052, PR China
[d] Department of Architecture and Civil Engineering, University of Bath, Claverton Down BA2 7AY, United Kingdom

ARTICLE INFO

Keywords:
MOF
MOF derivative
Solar cell
Dye-sensitized solar cell
Perovskite solar cell
Organic solar cell

ABSTRACT

The utilization of naturally existed energy is an indispensable solution to realise carbon neutral society in the future. Solar energy in the Sun is a tremendously abundant renewable and green energy resource which can provide more than enough energy to meet the whole world's demand. The biggest challenge is to develop cost-effective and durable materials to achieve efficient transformation of solar energy to electricity. As the most promising energy harvesting devices that based on the photovoltaic effect, solar cells can effectively transfer sunlight into electricity and the technologies have expanded rapidly over recent decades. Materials with optimal properties are the key to achieving efficient solar energy-driven performance for a variety of solar cells. Metal-organic frameworks (MOFs) and their derivatives, featured a great symbiosis of morphological, physicochemical and semiconducting properties that are difficult to achieve through the conventional materials, were intensively explored for energy storage and conversion applications in the past decade due to their intrinsic porous structures, tremendous inorganic-organic nature and fantastic diversity in functionalities. MOFs and derivatives based photovoltaic devices, especially solar cells, have demonstrated exceptional potential to enhance solar-to-electricity conversion performance with increased stability. In this review, the state-of-the-art progress on the applications of MOFs and their derivatives in a diverse range of solar cell devices including dye-sensitized solar cells, perovskite solar cells and organic solar cells is systematically documented. Important aspects on material compositions and structures, material synthesis strategies, device processing techniques, and photovoltaic performances of MOFs-based and MOF-derived materials used in solar cells are discussed and analyzed. The utilizations of MOFs and their derivatives as electrodes, photoactive materials, charge carriers and additives in different solar cells are highlighted. In addition, current challenges and perspectives on further development of MOF based materials for solar cell applications are also discussed.

1. Introduction

Energy crisis is one of the key challenges that mankind is currently facing. Renewable energy, which mainly includes solar energy, tidal energy and wind energy, has become an indispensable solution for future energy demands. Among different types of renewable energies, solar energy is the most important one because of its zero-pollution, resource-free and economical characteristics [1–3]. Solar cell is one of the most readily available energy conversion devices that can transfer solar energy to practically useable electricity. However, currently solar cells are not yet satisfactory due to their high cost, low efficiency and limited scale [4].

Nowadays, silicon-based solar cells are the most exploited and commercialized photovoltaic devices for the conversion of solar energy to electricity. The first silicon-based solar cell was developed by Bell Laboratories in 1954 with an efficiency of 6% [5], and now the highest efficiency reported is up to 27.6% [6]. Although silicon-based solar cells work well in outdoor conditions, they become inefficient indoors mainly because its bandgap does not match with the indoor illumination spectra [7], and the light intensity of indoor illumination is 300–3000 times weaker than that of outdoor sunlight [8]. Other emerging alternative technologies including dye-sensitized solar cells (DSSC) [9–12], perovskite solar cells (PSC) [13–15] and organic solar cells (OSC) [16–18] have drawn significant attention in the past years and are now

* Corresponding author.
E-mail address: y.xia@exeter.ac.uk (Y. Xia).

https://doi.org/10.1016/j.mser.2022.100714
Received 3 July 2022; Received in revised form 4 December 2022; Accepted 14 December 2022

considered as the new generation of solar cells.

Metal–organic frameworks (MOFs) are a class of fascinating porous materials formed via chemical interactions between metal ions and organic ligands [19,20]. MOFs can offer large specific surface area, high porosity, adjustable pore channels, and tailorable functionality [21,22]. They have been widely studied in many typical applications of porous materials, such as gas adsorption and storage [23,24], drug delivery [25, 26], catalysis [27–29], ion exchange and separation [30], and sensing [31,32]. Moreover, MOFs can provide an excellent platform to generate a variety of nanostructured MOF derivatives by thermal transformation. MOF derivatives, such as porous carbon-based materials, metals, metal oxides, metal chalcogenides (metal sulfides and selenides), metal phosphides and metal carbides as well as diverse carbon-based composite materials become attractive in many applications including catalysis, environment remedy, photocatalysis, energy storage and conversion [33–44]. However, the utilization of MOFs and their derivatives in photovoltaic devices, has received comparatively less attention than in their traditional applications, as a consequence the development of this area is still in its infancy [45–47].

Since the first report on the utilization of MOFs as active material in a fully devised solar cell in 2007 [48], much effort has been devoted to improving the performance efficiency of DSSC by optimizing the MOFs-based photoanodes and counter electrodes. The studies on MOF-sensitized solar cell have shown rapid growth and the terms "MOFSC" and "MSSC" were used in the papers published in 2016 and 2017, respectively [49–53]. Generally, MOFs can be utilized not only as an active material, host, interfacial modifier, or precursor in the photoanode, but also as an active site or conductive material in the counter electrode [54–60]. Moreover, since the optoelectronic properties of MOFs can be modulated through controlling the constituent metal ions and organic linkers, more recently the application of MOFs with high chemical and thermal stability in PSC has attracted considerable attention. MOFs and derivatives can generally be used in PSC as a support, electron and hole transport materials in interfacial layer (interlayer), electron transport layer, hole transport layer, and heterojunction perovskite/MOF layer [54–56, 59, 60]. However, unlike the fast development of use MOF-based and derived materials in DSSC and PSC, utilization of MOFs in OSC has been rarely studied [54–56]. Overall, the development of MOFs and their derivatives in solar cells is still in an early stage, and it is highly desirable to overview the recent progress and provide prospects for both MOFs and solar cells communities.

In recent years, several publications have partially reviewed the applications of either MOFs or MOF derivatives in solar cells. For instance, in 2016 Deep et al overviewed the advances in the photovoltaic applications of coordination polymers and MOFs [59] work using MOF as quasi-solid electrolytes and counter/working electrodes in DSSC, as well as MOFs in perovskite solar cells were reviewed. Later in 2019, Wu et al provided a summary of the progress in the applications of MOFs in DSSC, PSC, and OSC [54]. Kim also reviewed MOFs in PSC [55]. In addition, other papers partially reviewed the use of MOF derivatives in solar cells [55–57, 60, 61], such as the review of MOF-derived materials in solar cells by Verpoort et al [56]. However, to the best of our knowledge, so far, no dedicated reports are available to provide critical analysis and overview on the applications of both MOF-based and MOF-derived nanomaterials for different solar cells, which is pivotal for further design and development of novel nanomaterials for highly efficient next-generation solar cells. Considering the rapid development in this area, it is highly desirable to provide an updated comprehensive overview of both MOFs and their derivatives in different types of solar cell applications. In addition, providing the current challenges and perspectives in this area would be beneficial to relevant researchers and communities.

In this review, we analyze and discuss the recent progress of the emerging applications of MOFs based materials and derivatives in diverse solar cells. This review is divided into six parts: We first briefly summarize the general aspects on the synthesis and process of MOFs and derivatives for solar cell utilizations, followed by the introduction of the basic principle and main parts of different solar cells including DSSC, PSC and OSC. Then we analyze and summarize the state-of-the-art development on the utilization of MOFs and derivatives in these different solar cells. In particular, we discuss the preparation strategies, constituents and structure analysis as well as performance comparison of MOFs and derivatives used as the photoanode, current electrode or electrolyte in DSSC, as interfacial layer, electron transport layer, hole transport layer or heterojunction in PSC, and OSC respectively in details. Finally, we provide brief summaries with concluding remarks and discuss the outlooks of future development of MOFs and derivatives for solar cell applications.

2. General aspects on the synthesis and process of MOFs and derivatives

2.1. Synthesis of MOFs

The synthesis and applications of MOFs have been developed rapidly in recent decades [21,62,63], and it has become possible to control the surface area, porosity, network topology of MOFs, making MOFs to be adapted to the requirements of many specific applications. The synthesis of MOFs is determined by many factors including the nature of metal ions and organic ligands, as well as the types of synthesis methods used. Transition metal ions, especially those transition metal elements in the first row of the periodic table, lanthanides, and alkaline earth metal ions have been widely used for the synthesis of MOFs. This is mainly due to their wide variety of coordination numbers, oxidation states and geometries [64]. Typical organic ligand materials with carboxylate, phosphonate, or sulfonate groups are considered as the three representative coordinating ligands [65–67].

Generally, MOFs can be prepared via hydrothermal or solvothermal synthesis method. Usually, a mixture containing metal salt and organic solvents reacts with organic ligands under controllable conditions (i.e. synthesis temperature and time) to form targeted MOFs, with reaction time varying from several hours to days. The types of solvents, synthesis temperatures, synthesis time, concentrations of metal salts and organic ligands, and pH of the solution could modulate the crystallinity, particle size and particle morphology of the synthesized MOFs [68]. Moreover, alternative synthesis methods such as microwave-assisted [69,70], sonochemical [71,72], electrochemical [73,74], and mechanochemical [75,76] methods were also developed to achieve the reduction of synthesis time and to produce smaller and uniform MOF crystals. Main parameters that effect the formation of MOFs and the synthesis methods of MOFs are summarized in Table 1.

2.2. Synthesis of MOF derivatives

MOFs can be transferred into MOF derivatives such as porous carbons, metals, metal oxides, metal sulfides, metal selenides and metal phosphides as well as their hybrid materials using different MOF precursors and synthesis methods. The MOF precursors normally include two categories, which are self-templated MOFs and external-templated MOFs [34]. The self-templated MOFs are MOFs-only precursors, while external-templated MOFs are MOFs combined with external materials such as graphene, silica and metal oxides. The morphologies of MOF derivatives can be maintained from the self-templated MOFs. As external-templated MOFs generally prepared by mechanical mixing or in situ growth of MOFs on supporting external materials, the morphology of MOF derivatives usually depends on the external materials [77]. The structure of MOF derivatives can be divided into 0D, 1D, 2D, and 3D (D means dimension). Polyhedra, core/shell and hollow structures are considered as 0D structure; nanowires, nanorods, nanoshuttles, and nanotubes are 1D structure; nanoplatelets and nanosheets are regarded as 2D structure; and nanocages, nanocubes and nanosponges are categorized as 3D structure [78,79].

Table 1
Main parameters affecting the formation of MOFs or derivatives and their synthesis methods.

Main parameters affecting the formation of MOFs and derivatives	
MOFs	**MOF derivatives**
Choice of metal ions Choice of organic linkers Choice of synthesis methods	Choice of self-templated precursors Choice of external-templated precursors Choice of synthesis methods
Synthesis methods	
Hydrothermal or solvothermal method *Types of solvents, synthesis temperatures, synthesis time, concentrations of metal salts and organic ligands, and pH*	Thermal treatment method *Temperatures, ramp rates, pyrolysis time, and gaseous atmosphere*
Microwave-assisted method *Types of solvents, synthesis temperatures, synthesis time, concentrations of metal salts and organic ligands, pH, and microwave power outputs*	Reflux synthesis method *Temperatures, time, and solvents*
Sonochemical method *Types of solvents, synthesis temperatures, synthesis time, concentrations of metal salts and organic ligands, pH, and sonication power outputs*	
Electrochemical method *Types of solvents, synthesis temperatures, synthesis time, concentrations of metal salts and organic ligands, electrolyte, and voltage-current density*	Electrochemical fabrication method *Scan rates and potential range*
Mechanochemical method *Grinding time, and additional solvents*	

Thermal treatment is the most widely used method for the production of MOF derivatives. It normally subjects MOF precursors to high temperature under different gaseous atmospheres, including inert atmospheres such as Ar or N_2, oxidation atmospheres such as, air or water-vapour, and reduction atmospheres such as H_2S or NH_3. The morphologies, chemical compositions, and crystallinities of the MOF derivatives can be tuned by control over the thermal treatment conditions, including temperature, ramp rate, pyrolysis time, and gaseous atmosphere [80,81]. Moreover, other synthesis approaches were also developed to produce specific MOF derivatives. For instance, reflux synthesis method is used to heat up a chemical reaction mixture in a specific solvent, and reflux the solvent vapours at a constant temperature [81,82]. MOF derivatives can also be produced by electrochemical fabrication methods via control of scan rate and potential range at low temperature reaction conditions [81,83]. More synthesis details of MOF derivatives are also summarized in Table 1, and will be further discussed in later sessions.

2.3. Process of MOFs and derivatives for solar cell applications

As the applications of MOFs and derivatives in solar cells started in the last 10 years, most of the studies are focused on the performance and stability of the assembled solar cells. The process of MOFs and derivatives in solar cell applications is generally still limited to the lab scale. Spin coating is a widely used method for the preparation of MOFs and derivatives for solar cell applications in the laboratory [61,84,85]. Other techniques including layer-by-layer (LBL) deposition [86], atomic layer deposition (ALD) [53], and screen-printing [87,88] have also been reported for the integration of MOFs and derivatives into solar cells. With rapid development in the field, it is anticipated that more large-scale production roll-to-roll (R2R) methods such as knife coating, spray coating, inkjet printing and pad printing will be applied to achieve cost-effective MOFs and derivatives based solar cells in the future [89].

3. Basic principle of solar cells

Solar cells are energy conversion devices based on the photovoltaic effect that convert solar energy from the sun into electrical energy. The photovoltaic effect takes place if the carriers, which are either electrons or holes, become excited and generate voltage or current when the material is irradiated by sunlight. Generally, a solar cell contains a semiconductor material where the nature of the bandgap determines the performance. Different semiconductor materials with variable bandgaps can absorb photons of the sunlight with different energies from UV to deep infrared. If the bandgap of a semiconductor material matches the wavelengths of light shining on the solar cell, the solar cell can then efficiently make use of the available energy of sunlight [90]. Power conversion efficiency (PCE) of solar cells is the most important indicator to measure the solar-to-power efficiency of a solar cell, which is determined by three key parameters, open-circuit voltage (V_{oc}), short-circuit current (J_{sc}) and fill factor (FF). V_{oc} is the potential difference from both ends of a solar cell upon light irradiation under open circuit. V_{oc} is normally dictated by the bandgap of the semiconductor material, where a large semiconductor bandgap results in a high value of V_{oc}. FF is defined as the ratio of the maximum power from the solar cell (P_{max}) to a solar cell of V_{oc} and J_{sc}, with the equation: $FF = P_{max} / (V_{oc} \times J_{sc})$. Graphically, FF is a measure of the "squareness" of the solar cell in the current density–voltage (J–V) curve. It indicates how close the J–V curve is to a rectangle under light irradiation [91]. PCE is defined as the ratio of energy output from the solar cell to input energy from the Sun (P_{input}). PCE can be calculated using the equation: $PCE = V_{oc} \times J_{sc} \times FF/P_{input}$.

Three generations of solar cells have been developed so far. The first-generation solar cells are crystal silicon based solar cells that can be divided into monocrystalline and polycrystalline silicon solar cells depending on the crystallinity of silicon. Among them, single-crystal silicon solar cells exhibit the highest PCE, but the fabrication process cost is high [92]. The development of the second-generation solar cell is focused on thin-film construction, which can deliver comparable PCE with less material consumption and reduced cost. As a typical semiconductor compound, copper indium gallium selenide (CIGS) has been the mainly studied material [93]. A CIGS thin-film solar cell with a thickness of 1–2 μm could be manufactured at a relatively low cost in comparison with those based on silicon [94]. The latest third-generation solar cells are mainly based on novel semiconducting materials such as organic macromolecules, inorganic nanoparticles and hybrids [95,96]. The third-generation solar cells are considered to have promising potentials of high PCE, low-cost and large-scale development. The emerging third-generation solar cells include not only DSSC, PSC, OSC, but also quantum dot (QDSC) [97] and the copper zinc tin sulfide solar cell (CZTS) [98]. In this review, we mainly focus on the utilization of MOFs and their derivatives in third-generation solar cells DSSC, PSC and OSC.

DSSC, also known as the "Grätzel cell", has attracted great attention over the past 30 years due to its silicon-free nature [99]. A typical DSSC contains four major parts – photoanode, counter electrode, dye and electrolyte. The photoanode in a DSSC functions as the carrier of the dye and plays an important role in transporting electrons. The most widely studied photoanode material is TiO_2, but other materials such as ZnO and SnO_2 have also been explored [100]. The counter electrode (CE), also called photocathode, plays the main function of collecting electrons conducted by the photoanode from the external circuit and reducing the ion oxidation state within the electrolyte. A platinum electrode is normally adopted as the CE. A dye, commonly based on ruthenium complexes are used to absorb and convert sunlight so as to realize the flow of electrons in the DSSC. An electrolyte, usually iodide/tri-iodide (I^-/I_3^-), then fulfils the function of reducing the dye molecules from the oxidized state to the ground state, enabling their continuous regeneration [11]. A typical schematic diagram of a dye-sensitized solar cell is presented in Fig. 1a. The state-of-the-art DSSCs have been reported to achieve PCE of 15% in lab scale [101]. A high PCE of 28.9% achieved using indoor lighting in a DSSC can be realised by using Cu(II/I)$(tmby)_2$ (tmby, 4,4′,6,6′-tetramethyl-2,2′-bipyridine) as the redox mediator, and the two judiciously designed XY1 and D35 as sensitizers [1].

DSSC devices transform solar energy to electricity via the following reaction processes including light absorption, charge generation and

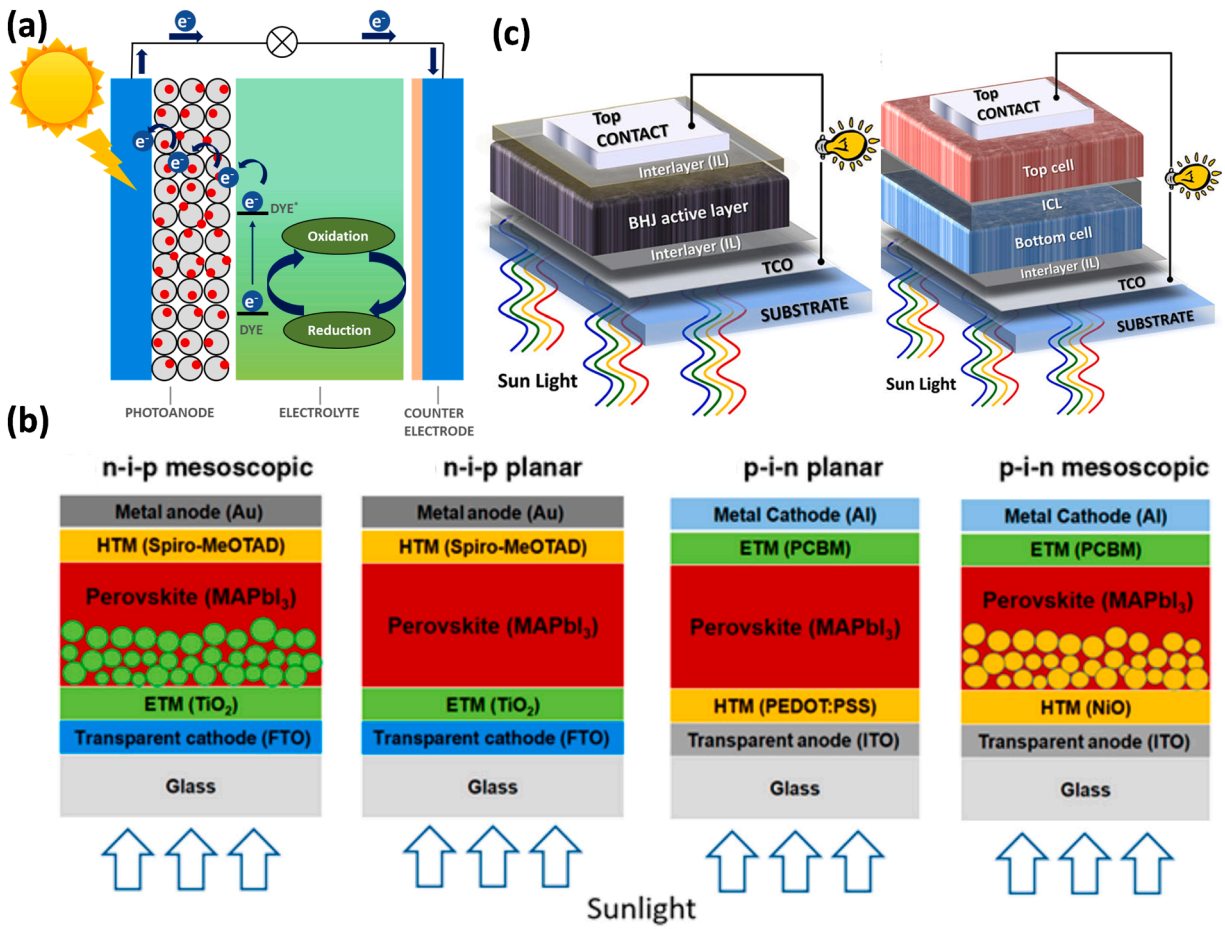

Fig. 1. Schematic diagram of (a) a dye-sensitized solar cell, (b) perovskite solar cells with four structures. Reproduced with permission [114]. Copyright 2016, Society of Photo-Optical Instrument Engineering (SPIE). (c) Schematic diagram of a single-junction OSC (left) and a tandem solar cell (right). Copyright 2021, Wiley-VCH GmbH [89].

charge transfer [102]:

(1) The incident light is irradiated from the photoanode in the solar cell, and the dye adsorbed on the photoanode captures the sunlight and transitions from the ground state (S) to excited state (S*), namely $S + h\gamma \rightarrow S^*$;
(2) The dye in the excited state (S*) injects electrons into the conduction band of the semiconductor, and the dye molecule loses electrons and is oxidized to state (S^+), which can be expressed as $S^* \rightarrow S^+ + e^-$;
(3) The injected electrons are transferred to a conductive substrate through the conduction band, and then transferred to the external circuit through a conductive substrate before flowing from the external circuit to the counter electrode;
(4) The dye molecules in the oxidation state are reduced to the ground state by I^- in the electrolyte, and at the same time I^- is oxidized to I_3, described by the equation $2S^+ + 3I^- \rightarrow 2S + I_3^-$;
(5) I_3^- is reduced to I^- by the electrons on the counter electrode, thus realising a complete photoelectric conversion cycle, namely $I_3^- + 2e^- \rightarrow 3I^-$.

Apart from DSSC, PSC has recently attracted increasing attention around the world because of its excellent photovoltaic performance. Throughout the past two decades, continuous efforts have been made to dramatically improve the PCE of PSC from 3.8% to 25.7% [103]. PSC usually comprises a conductive substrate (fluorine-doped tin oxide (FTO) or indium tin oxide (ITO)), an electron transport layer (ETL), a hole transport layer (HTL), a light absorber (i.e. perovskite layer) and a metal electrode. As shown in Fig. 1b, PSC is primarily divided into mesoscopic and planar structures and can be further classified into standard (n–i–p) and inverted (p–i–n) configurations. For mesoporous structures, perovskite is loaded into a mesoporous skeleton, which is helpful to form a uniform perovskite film and beneficial to the electron transport. TiO_2 has been widely investigated as an ETL in PSC and mesoporous TiO_2 with n-i-p structures is the most common configuration for high efficiency PSCs. In terms of planar structures, the perovskite is surrounded by the HTL and ETL [61].

The power generation mechanism of PSC can be divided into two steps: light absorption and generation of electron-hole pairs, followed by the dissociation and transport of carriers. In the first step, after absorbing light, excited electrons in the light adsorbed materials are transferred from the valence band to the conduction band. An electron-hole pair is then produced as the valence band contains positively charged holes. Due to the indirect band of perovskite crystal structures, in which the valence band and the conduction band correspond to different wave vectors, indirect transition processes will occur accompanied by electron-photon interaction. Such indirect band-gap materials have significantly lower light absorption coefficients than direct band-gap materials [61]. However, organic-inorganic metal halide perovskites such as $CH_3NH_3PbI_3$ has a low binding excitation energy, enabling the formation of electron-hole pairs [104]. In the second step, the electron-hole pairs photogenerated from perovskite are then dissociated and extracted into ETL and HTL, further generating photocurrent and photovoltage. The photoelectric performance of a PSC is determined by the carrier mobility of the perovskite. It is worth mentioning that the recombination of holes and the recombination of electrons among the

perovskite layer, HTL and ETL are non-ignorable, which can negatively influence the photoelectric performance [61]. Therefore, improving the yield of electron-hole pairs and preventing the recombination of holes or electrons are hot topics in PSC research.

The development of PSC is extremely fast, and its world record efficiency was frequently broken in the last 10 years. A high PCE of 25.7% for PSC was achieved by a group of Korean scientists [103], which was also certified by the National Renewable Energy Laboratory, US. Currently, the highest PCE record exceeds the 30% efficiency barrier with a value of 31.3%, which was realised by a perovskite-on-silicon tandem solar cell [105,106].

In terms of OSC (Fig. 1c), organic materials are employed as a semiconductor to produce electricity from the Sun. OSCs are made with organic compounds that can be dissolved in ink and printed onto thin plastics, enabling easy and cost-effective manufacture. Techniques such as printing, spin coating, and spray deposition are applied to manufacture OSCs. The PCE of OSCs has been boosted to over 18% recently [107–112]. The state-of-the-art OSC can achieve a high PCE of 19.0% [112]. This OSC has a rationally designed active layer comprising a new wide-bandgap polymer donor (PBQx-TF) and a new low-bandgap non-fullerene acceptor (eC9–2Cl) [112]. However, the value of PCE is still relatively low compared with other types of solar cells. The efficiency limitation and long-term stability of OSCs remain significant barriers for their practical applications. To alleviate the intrinsic transmission loss and thermalization loss in single-junction OSCs (left in Fig. 1c), two different donor materials with complementary absorption spectra can be combined in a single layer device or used as two individual active blends of sub-cells connected in a multifunction tandem OSCs (right in Fig. 1c).

In order to achieve the functions of charge collection and transport, one electrode of the OSC must be transparent so that the solar photons can be utilized by the active layers. Metals such as aluminium and silver can be used as the other electrode, since they reflect unabsorbed light for secondary utilization. The light-harvesting layer, which can be a blend of donor and acceptor materials or two separated donor and acceptor layers, is undoubtedly playing the most important role in OSCs. It can absorb solar photons and convert them to free charge carriers [113].

4. Applications in dye-sensitized solar cells

In conventional dye-sensitized solar cells (DSSCs), metal oxide semiconducting materials such as TiO_2, Nb_2O_5, and ZnO are usually used as photoanodes, with only a small fraction of light in the UV region absorbed, thus photosensitive molecular sensitizers are frequently required to improve DSSC performance [115]. A desirable photoanode material usually has (1) appropriate band positions; (2) large surface area for dye loading; and (3) open pore structure for dye sensitization and transport of redox couple [115]. Moreover, a photosensitizer or dye material should possess properties including (1) luminescent property that can emit light during the process of returning from the excited state to the ground state after being excited by external light; (2) coverage of ultraviolet-visible (UV–vis) and near-infrared region (NIR) regions in the absorption spectra and (3) appropriate value of highest occupied molecular orbital (HOMO) and lowest unoccupied molecular orbital (LUMO) to match the photoanode and redox. The LUMO should be close to but higher than the conduction band of the photoanode, while the HOMO level should be lower than that of redox [115]. In addition, counter electrode (CE) materials in DSSC can catalyse the reduction of I^-/I_3^- liquid electrolyte or other redox couples.

To be used as photoactive materials in DSSCs, MOFs and derivatives should exhibit proper light harvesting capability, ranging from visible light to NIR. Since the light-harvesting window of photoactive materials is generally determined by its bandgap, the choice of a MOF with a suitable bandgap that can absorb light is essential to allow it to be functioned as a photoactive material. Moreover, the porous structures, together with the chemical and thermal stability of MOFs also play vital role for MOFs to be used as functional additives or interlayers to improve the performance and stability of DSSCs.

MOF-based materials have been widely explored not only as active materials, hosts or interfacial modifier in photoanode for DSSCs, but also as active components or conductive materials in counter electrodes [54–60]. Moreover, MOFs have also been explored to form MOF-polymer or MOF-gel as electrolytes in DSSC. In addition, MOF-derived materials have also attracted interest as both photoanode and counter electrode materials in DSSCs. Recent advances in the applications of MOF-based and derived materials in DSSC are overviewed in this part.

4.1. Utilization of MOFs as sensitizers in DSSCs

4.1.1. Pristine MOFs as sensitizers in DSSCs

Han's group has been active in the research of MOFs as photosensitizers in DSSCs. Initially, they fabricated thin layer Cu-BTC MOFs (copper(II) benzene-1,3,5-tricarboxylate) using a layer-by-layer (LBL) deposition technique.[86] Through iodine-doping to Cu-BTC MOF, the Cu-BTC was made electrically conductive, enabling the iodine-doped Cu-BTC (I_2@Cu-BTC) to be used as a sensitizing layer in TiO_2-based DSSCs. They then introduced multi-walled carbon nanotubes (MWCNT) into the Cu-BTC sensitized DSSC [116]. The electron transfer of the as-fabricated DSSC was improved, and the PCE of this DSSC was enhanced by up to 60%. Similarly, they also investigated the feasibility of ruthenium-based MOF (Ru-BTC) films and two cobalt-based MOF (cobalt-naphthalenedicarboxylic acid, Co-NDC, and cobalt-benzene dicarboxylic acid, Co-BDC) films as photosensitizers in DSSCs [117,118]. The HOMO-LUMO energy states of the as-prepared MOF films were estimated to be suitable to allow their use as sensitizers for TiO_2. Since the HOMO level of Ru-MOFs film was estimated to be − 5.47 eV vs. vacuum, while its LUMO level was calculated as − 3.21 eV vs. vacuum that is higher than the conduction band of TiO_2 (−4.2 eV vs. vacuum), which makes Ru-MOFs films desirable sensitizers [117]. Moreover, the HOMO energy states of MOFs Co-BDC and Co-NDC were estimated to be − 6.22 eV vs. vacuum, and the LUMO energy states were calculated to be about − 3.95 eV vs. vacuum. Therefore, the HOMO-LUMO energy states of the MOFs Co-BDC and Co-NDC make them suitable as sensitizers in a TiO_2 based DSSC [118]. The iodine doping was found to be important to facilitate the electron transfer between the interfaces of MOFs and TiO_2. In addition, Han et al. designed another type of cobalt-based MOF (Co(II) di(3-diaminopropyl)-viologen, Co-DAPV) as a photosensitizer, which is suitable for TiO_2-based solid-state DSSCs with a PCE value (η) of 2.1% [119].

Apart from the MOFs as sensitizers reported by Han's group, a range of other MOFs have also been studied as sensitizers for photoanodes in DSSCs. For example, porphyrin and its derivatives can be used as sensitizers in solar cells due to their large photoabsorption coefficients under visible light. Liu et al. prepared thin films consisting of different types of porphyrinic MOFs grown on conducting substrates (SURMOFs), which was used as the photoanodes in DSSCs [120–122]. Despite the high values of J_{sc} and V_{oc}, their corresponding total efficiencies of 0.017% and 0.006% for DPA-Zn(II)porphyrin Zn-SURMOF 2 and Zn(II) porphyrin Zn-SURMOF 2, respectively [121] are rather low. Similarly, Morris et al. solvothermally prepared a series of zirconium based MOF UiO-67 (Zr) (Universitetet i Oslo) films which incorporated various ruthenium(II) polypyridyl ligands (RuDCBPY) as the photosensitizers in DSSCs [51]. Fig. 2a-b show the schematic illustrations of the difference between the conventional DSSC and the RuDCBPY@UiO-67 sensitized DSSC. By using RuDCBPY@UiO-67 as a sensitizer, the dyes are expected to be distributed spatially and uniformly over the surface of the TiO_2 throughout the pore channels of the UiO-67 matrix. It was claimed that although the efficiency of DSSCs prepared by RuDCBPY@UiO-67 was less than 1% (i.e. 0.123%), they're still promising as performance improved compared to a reference TiO_2 evaluated under the same conditions [51]. Pillared porphyrin framework (PPF) is another MOF

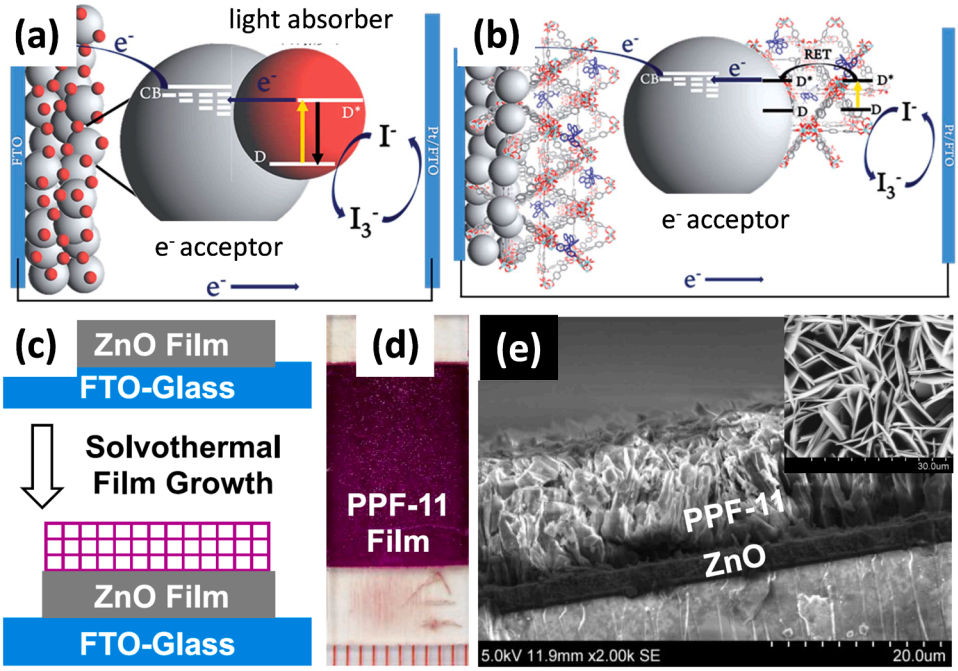

Fig. 2. Schematic diagram of (a) a conventional DSSC, and (b) RuDCBPY@UiO-67/TiO_2 sensitized DSSC. Reproduced with permission [51]. Copyright 2016, Royal Society of Chemistry. (c) Schematic diagram of the solvothermal growth of PPF-11 film on the surface of ZnO film/FTO-Glass substrate; (d) Photograph of PPF-11/ZnO film and (e) Cross-sectional SEM image of PPF-11 film with 10 μm thickness on ZnO layer. The inset image is the top view showing the dense-packed PPF-11 crystals aligned on the surface. Reproduced with permission [123]. Copyright 2019, American Chemical Society.

sensitizer material, which was coated on the TiO_2 substrate via atomic layer deposition (ALD) by Spoerke et al [53]. In addition, Gordillo et al. also solvothermally grew the (100) -oriented PPF-11 films onto a ZnO/FTO substrate (Fig. 2c-d) [123], and the SEM image (Fig. 2e) clearly showed the 10 μm thick PPF-11 film formed on a 2.5 μm thick of ZnO layer. This as-prepared (100) oriented PPF-11/ZnO−FTO photoanode exhibited good photovoltaic performance with a PCE value of 0.82%, which is higher than that previously reported for RuDCBPY--based [51] (i.e. η is 0.123%) and porphyrin MOFs [53] based (i.e. η is 0.0023%) cells. In addition, other types of MOFs including chiral heterometallic In(III)−K(I) MOFs [124], MOF-199 [52], and graphene-Eu-MOF [125] have also been reported to be used as photosensitizer materials in DSSCs. It is worth noting that although the efficiency of most DSSCs fabricated with MOF-based sensitizers is low (normally < 1%), it is still higher than that of the DSSCs fabricated without using MOFs under the same conditions, implying the potential of using pristine MOFs as sensitizers for photoanodes to enhance the PCE of DSSCs.

4.1.2. TiO_2-MOFs based nanocomposites as sensitizers in DSSCs

TiO_2-MOFs nanocomposites have been investigated as sensitizers for photoanodes in DSSCs. For example, Shajan et al. prepared TiO_2-MOF aerogel composite, TiO_2-[Zn(N-(4-pyridylmethyl)-L-valine·HCl)(Cl)] $(H_2O)_2$ via a sol-gel method, and tested its feasibility as photoanode in a quasi-solid dye-sensitized solar cell (QSDSSC) [126]. Later, by using the same sol-gel method, they also prepared TiO_2-Ni-BTC MOFs (nickel(II) benzene-1,3,5-tricarboxylate) aerogel composite [127,128] and TiO_2--Cu-BTC MOFs aerogel composite [128]. When the TiO_2-Ni-BTC was applied in the photoanode, the fabricated QSDSSC could achieve a promising PCE value of 8.846% [127]. Apart from using a chemical synthesis method to prepare the composites, TiO_2-Zn-BTC and ZnO-UiO-66 composite powders were also prepared using a mechanical mixing method [129,130] where various amounts of Zn-BTC or UiO-66 were added into TiO_2 particles to optimize the composite as the photoanode in DSSCs.

4.2. Utilization of MOFs and derivatives as photoanodes in DSSCs

4.2.1. MOFs as photoanodes in DSSCs

The first study on the application of MOFs as photoanodes in DSSCs was reported by Garcia et al. in 2011. They investigated the intrinsic photoresponse of four commercially available MOFs and found only one MOF film composed of $Al_2(BDC)_3$ (BDC is p-benzenedicarboxylate) was active in a photovoltaic device. It is therefore anticipated that $Al_2(BDC)_3$ could be potentially used as the photosensitizing material in DSSCs [49]. Ever since then, studies on MOF-based photoanodes for DSSCs have increased. Garcia et al. also studied the photocatalytic performance of NH_2 −UiO-66(Zr/Ti) prepared with different contents of Ti, and found the substituted Ti acted as mediator to facilitate electron transfer, leading to a higher photon-to-current efficiency compared to NH_2 −UiO-66(Zr) [131].

MOFs can also be utilized as interfacial modifiers for photoanode in DSSCs, since MOFs usually have high specific surface area excessing 1000 $m^2\ g^{-1}$, as well as tuneable pore morphology, which enable a significant amount of dyes to be loaded into MOFs for photoanode applications. In 2011, Wei et al. intended to enhance the V_{oc} of DSSCs by coating a thin layer of ZIF-8 (Zeolitic Imidazolate Framework) onto the TiO_2 [132], but found that the J_{sc} decreased following ZIF-8 coating. In order to solve this problem, his group proposed a facile post-surface treatment method (Fig. 3a) [133], which enabled the TiO_2 photoanode to adsorb dyes tightly and consequently both J_{sc} and V_{oc} increased [133]. Zhao et al. demonstrated that ZIF-8 coated TiO_2 (Fig. 3b) exhibited enhanced photovoltaic performance under the redox mediator of tris(2,2'-bipyridine) cobalt(II)/(III), which resulted in a PCE of 9.42% [134]. Moreover, He et al. reported the modification of ZIF-8/TiO_2 photoanodes by the introduction of a three-dimensional graphene network (3DGN) [135] and reduced graphene oxide (RGO) [136] into the TiO_2. 3DGN can not only bring a fast electron transport ability to depress the loss of electrons, but also a high electronic conductivity [135], while RGO can provide a better electron transport network and improve the conductivity of the photoanode [136]. For example, as shown in Fig. 3c, the specific photocurrent value of ZIF-8 modified TiO_2 photoanode is 5.74 times higher than that of pure TiO_2, suggesting a fast and uniform photocurrent response for DSSCs [136]. Such highly conductive carbon-based additives are expected to enhance the

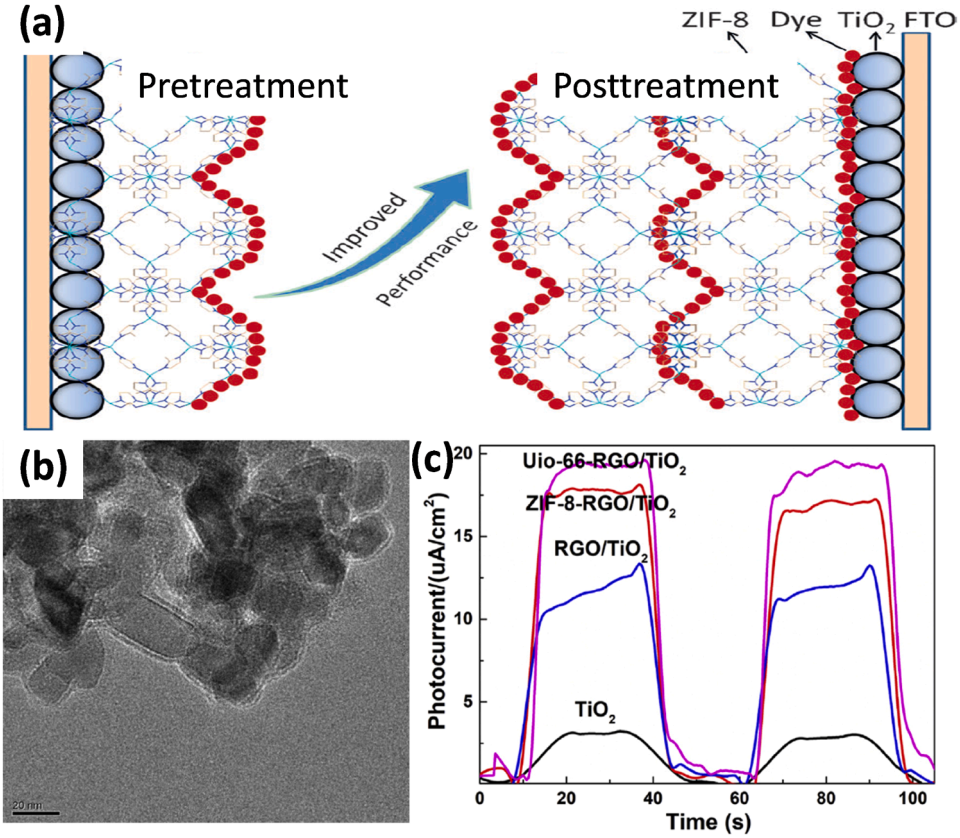

Fig. 3. (a) Schematic diagram of the possible photoanode statuses after pre-treatment and post-treatment methods. Reproduced with permission [133]. Copyright 2014, Wiley-VCH GmbH. (b) HR-TEM image of TiO_2 nanoparticles coated with ZIF-8 layer. Reproduced with permission [134]. Copyright 2017, Elsevier B.V. (c) Photocurrent signals of photoanodes with or without the modification of RGO and MOFs. Reproduced with permission [136]. Copyright 2020, Elsevier B.V.

photo-induced electron transport ability of ZIF-8/TiO_2 photoanodes, resulting in significantly improved photovoltaic performance. The J_{sc}, V_{oc}, PCE and other parameters of MOF-based DSSCs mentioned above are summarized in Table 2.

4.2.2. MOF derivatives as photoanodes in DSSCs

4.2.2.1. MOF-derived TiO_2-based photoanodes. Since MOFs are porous materials constructed from metal ions and organic linkers, they can be readily used as precursors for the preparation of numerous metal compounds or metal compound/carbon-based composites as photoanode in DSSCs. Wei et al. first reported the synthesis of hierarchical porous TiO_2 powder by simple thermal heating MIL-125 (Ti) (Matériaux de l'Institut Lavoisier) at 380 °C for 5 h in air [138]. The as-synthesized TiO_2 was then applied as a photoanode in a test DSSC device that exhibited a PCE of 7.20%. Kim et al. used a similar calcination method to convert MIL-125 (Ti) into TiO_2 with mesoporous structure [139,140]. They used either poly(ethylene glycol) diglycidyl ether (PEGDGE) [139] or poly (vinyl chloride)-graft-poly(oxyethylene methacrylate) (PVC-g-POEM) [140] as the structure directing agent to precisely control the shape and morphology of the precursor MIL-125(Ti), consequently realizing the control over the morphology that results in the creation of hierarchical TiO_2. The hierarchical TiO_2 was fabricated as a photoanode in DSSC, and the device showed a higher PCE value than that of those fabricated with the benchmark TiO_2. This enhanced efficiency was attributed to the high surface area and high porosity of the hierarchical mesoporous TiO_2 derived from Ti-MOF, which is beneficial to the dye loading and photo-electron transfer.

To further improve the power conversion efficiency of DSSCs, researchers attempted to couple active materials with MOFs to obtain TiO_2-based nanocomposites [141–143]. For instance, Yin et al. synthesized Cu_2ZnSnS_4 (CZTS) nanoparticles (NPs) sensitized MIL-125 (Ti)-derived TiO_2 with mesoporous structure by a two-step hot injection and hydrothermal method (Fig. 4a) [141]. TEM images in Fig. 4b-c show the homogenous dispersion of CZTS NPs in TiO_2, and the high-resolution TEM (HRTEM) image (Fig. 4d) revealed a particle size of approximately 8 nm and lattice spacing of 0.33 and 0.24 nm indexed to the (100) and (004) planes of CZTS and TiO_2, respectively. The selected area electron diffraction (SAED) pattern (Fig. 4e) shows a good match with the planes of both CZTS and TiO_2 [141]. Due to the synergistic effect between mesoporous TiO_2 and CZTS nanoparticles, the DSSC based on CZTS/MIL-125 (Ti)-derived TiO_2 photoanode achieved a high PCE of 8.10%. A charge-transfer process for the CZTS/TiO_2-based DSSC was proposed (Fig. 4f) to explain the high suppression of the photoinduced exciton recombination and high ability to transport interfacial carriers [141]. Yin et al. also used hydrothermally synthesized layered MoS_2 coupled with MIL-125 (Ti)-derived dual-phase TiO_2 as a photoanode for DSSCs [142]. The coupling of layered MoS_2 improved the visible light response and therefore enhanced the photoelectric performance. As a result, the MoS_2/dual-phase TiO_2 displayed a very high PCE of 8.96%. In addition, Wang et al. designed two polyoxometalate (POM)-based MOFs, $[Ni(bpp)(H_2O)_2]_3[P_2W_{18}O_{62}]\cdot 24\ H_2O$ and $H_6[Cu_3(H_2O)_6(P_2W_{18}O_{62})_2\cdot 3\text{-dpye})_6]\cdot 28\ H_2O$, where POM acted as the secondary building units of MOFs to prepare TiO_2-based photoanodes [143]. After calcination of the as-synthesized MOFs together with the TiO_2 precursor at 500 °C in air, small-sized POM nanoparticles were highly dispersed into the TiO_2, enhancing the PCE of the DSSC up to 7.56%.

4.2.2.2. MOF-derived ZnO-based photoanodes. Apart from TiO_2, ZnO is also an excellent semiconductor that can be applied as a photoanode in DSSCs, due to its wide band gap [144,145]. Banerjee et al. first

Table 2
Summary of the performance of MOF-based materials as photoanodes in DSSCs.

MOFs	MOF photoanode	Cell type*	J_{sc} (mA cm^{-2})	V_{oc} (V)	FF	PCE (η, %)	PEC_{ref}, (η, %)	Ref.
$Al_2(BDC)_3$	DMB@$Al_2(BDC)_3$	SS	0.0362	0.36134	0.4046	N/A	N/A	[49]
NH_2 −UiO-66 (Zr/Ti)	NH_2 −UiO-66(Zr/Ti)	SS	0.06535	0.88562	0.5952	0.034	N/A	[131]
$[Cu_2(BDC)_2(BPY)]_n$	I_2 @ $[Cu_2(bdc)_2(bpy)]_n$ /TiO_2	LJ (I^-/I_3^-)	0.323	0.54	0.407	0.071	N/A	[137]
Porphyrin Zn-SURMOF 2	Pt@Porphyrin Zn-SURMOF 2	LJ (I^-/I_3^-)	0.71	0.7	0.65	0.45	N/A	[120]
Porphyrin Zn-SURMOF 2	DPA@Porphyrin Zn-SURMOF 2	SS	0.0529	0.86	N/A	0.017	N/A	[121]
Zn-perylene SURMOF	Zn-perylene SURMOF -Bodipy/ PMMA/TiO_2	LJ (Co^{2+}/Co^{3+})	0.0172	0.072	0.35	0.1185	$\eta_{without\ MOF} = 0.0246$	[122]
UiO-67(Zr)	RuDCBPY@UiO-67/TiO_2	LJ (I^-/I_3^-)	0.446	0.480	0.55	0.123	$\eta_{RuDCBPY-TiO2} = 0.077$	[51]
PPF-4	Porphyrin PPF-4 /TiO_2	LJ (I^-/I_3^-)	0.0085	0.515	0.521	0.0023	$\eta_{TiO2} = 0.0011$	[53]
[100]-oriented PPF-11	[100]-oriented PPF-11/ZnO	LJ (I^-/I_3^-)	4.20	0.47	0.41	0.82	$\eta_{ZnO-} = 0.17$	[123]
$[In_{0.5}K(3qlc)Cl_{1.5}(H_2O)_{0.5}]_{2n}$	$[In_{0.5}K(3qlc)Cl_{1.5}(H_2O)_{0.5}]_{2n}$/ N719/$TiO_2$	LJ (I^-/I_3^-)	17.79	0.74	0.61	8.07	$\eta_{N719/TiO} = 6.61$	[124]
$[InK(ox)_2\text{-}(H_2O)_4]_n$	$[InK(ox)_2\text{-}(H_2O)_4]_n$ /N719/TiO_2	LJ (I^-/I_3^-)	16.54	0.73	0.62	7.42	$\eta_{N719/TiO2} = 6.61$	[124]
MOF-199	DHBA/MOF-199 /TiO_2	LJ (I^-/I_3^-)	0.0285	0.416	0.475	0.005	$\eta_{ref} = 0.002$	[52]
Eu-MOF	Graphene-Eu-MOF /TiO_2	LJ (I^-/I_3^-)	20	0.449	0.44	2.3	N/A	[125]
Cu-BTC	I_2 @Cu-BTC/TiO_2	LJ (I^-/I_3^-)	1.25	0.49	0.43	0.26	$\eta_{no\ doping} = 0.008$	[86]
Cu-BTC	I_2 @Cu-BTC /MWCNT/TiO_2	LJ (I^-/I_3^-)	1.95	0.48	0.51	0.46	$\eta_{P25} = 0.20$	[116]
Ru-BTC	I_2 @Ru-BTC/TiO_2	LJ(I^-/I_3^-)	2.56	0.63	0.63	1.22	$\eta_{no\ doping} = 0.06$	[117]
Co-NDC	I_2 @Co-NDC/TiO_2	LJ (I^-/I_3^-)	2.56	0.63	0.63	1.12	$\eta_{no\ doping} = 0.003$	[118]
Co-BDC	I_2 @Co-BDC/TiO_2	LJ (I^-/I_3^-)	2.13	0.62	0.62	0.96	$\eta_{no\ doping} = 0.003$	[118]
Co-DAPV	Co-DAPV/TiO_2	SS	4.92	0.67	0.57	2.1	N/A	[119]
[Zn(N-(4-pyridyl methyl)-L-valine HCl) (Cl)]$(H_2O)_2$	TiO_2–MOF aerogel composite	QS	6.22	0.68	0.553	2.34	$\eta_{TiO2} = 3.08$	[126]
Ni-BTC	TiO_2-Ni-BTC aerogel composite	QS	27.32	0.624	0.516	8.846	$\eta_{TiO2} = 6.805$	[127]
Ni-BTC	TiO_2-Ni-BTC aerogel composite	QS	8.88	0.60	0.439	2.34	$\eta_{TiO2} = 0.97$	[128]
Cu-BTC	TiO_2-Cu-BTC aerogel composite	QS	1.70	0.32	0.236	0.13	$\eta_{TiO2} = 0.97$	[128]
Zn-BTC	TiO_2-Zn-BTC composite	LJ (I^-/I_3^-)	N/A	N/A	N/A	0.67	$\eta_{TiO2} = 0.45$	[129]
UiO-66(Zr)	ZnO-UiO66 composite	LJ (I^-/I_3^-)	4.12	N/A	N/A	N/A	N/A	[130]
ZIF-8	ZIF-8/TiO_2	LJ (I^-/I_3^-)	10.28	0.753	0.69	5.34	$\eta_{P25} = 5.11$	[132]
ZIF-8	ZIF-8/post-treated TiO_2	LJ (I^-/I_3^-)	10.89	0.789	0.739	6.35	$\eta_{untreated} = 5.84$	[133]
ZIF-8	ZIF-8/TiO_2	LJ (Co^{2+}/Co^{3+})	14.39	0.897	0.73	9.42	$\eta_{TiO} = 7.75$	[134]
ZIF-8	ZIF-8/3DGN/TiO_2	LJ (I^-/I_3^-)	20.9	0.681	0.616	8.77	$\eta_{TiO} = 4.55$	[135]
ZIF-8	ZIF-8-RGO/TiO_2	LJ (I^-/I_3^-)	17.8	0.679	0.606	7.33	$\eta_{TiO} = 4.55$	[136]
UiO-66	UiO-66-RGO/TiO_2	LJ (I^-/I_3^-)	18.6	0.678	0.608	7.67	$\eta_{TiO} = 4.55$	[136]

*Where SS, QS, and LJ are solid-state solar cell, quasi-solid solar cell and liquid-junction solar cell, respectively.

attempted to prepare rod-shaped and hexagonal-shaped ZnO microparticles by a simple one-step thermolysis of two Zn-based MOFs, [Zn(l-L_{Cl})(Cl)](H_2O) and [Zn(l-L_{Br})(Br)](H_2O), and the as-fabricated ZnO as photoanode in DSSC showed a low PCE of 0.15% and 0.14%, respectively [146]. Wei et al. printed a MOF-5 precursor onto a ZnO film, then calcined the printed film to obtain a hierarchical ZnO parallelepiped coupled ZnO film [147]. The as-calcined ZnO parallelepipeds were used as an effective scattering layer to improve the DSSC performance. Similarly, Wang et al. synthesized leaf-like-shaped MOF, ZIF-L hydrothermally, on the surface of a FTO substrate at room temperature (Fig. 4g) [148]. After calcination at 550 °C, ZIF-L crystals were successfully converted into ZnO nanosheets arched on the FTO substrate (Fig. 4h). The TEM image in Fig. 4i clearly shows that the ZnO nanosheets consisting of interconnected small nanoparticles. The lattice fringes are clearly identified indicating a lattice distance is approximately 2.60 Å, which is attributed to the d-spacing of (002) plane of ZnO crystals [148]. The ZnO film produced was applied as a photoanode in an as-fabricated cell that achieved a PCE of 2.52%. In addition, ZnO aggregates derived from ZIF-8 were also studied for the applications in DSSCs by Fujihara et al. [149]. The photoanode exhibited a PCE value of 3.37% due to its favourable nano/microstructure. Although MOF-derived ZnO-based materials as photoanodes in DSSCs show relative lower PCE performance values in comparison to TiO_2-based ones, it is believed their PCE performance can still be improved. This is because different morphologies of ZnO could affect its bandgap energy and flat-band energy. As a result, effective control of MOF derivative morphology is an important area for future investigation. The power conversion efficiency and other important parameters of MOF-derived materials as photoanodes for DSSCs in the reported literature are summarized in Table 3.

4.2.3. Summary

The applications of MOF materials as photoanodes in DSSCs have been demonstrated in four different aspects: (1) MOFs can be used as photosensitizers to sensitize, harvest and convert solar energy to electricity; (2) MOFs can be utilized as hosts for other active materials or sensitizers, which is known as Guest@MOF; (3) MOFs may be functioned as an interfacial photoanode modifier to improve the photovoltaic performance and (4) MOFs are excellent precursors for the production of metal oxides such as TiO_2 and ZnO as photoanodes in DSSCs. The first application (i.e. used as photosensitizer) could be the most challenging among the four different applications since most MOFs possess insulating characteristics due to the presence of redox-inactive organic ligands and the poor electronic overlap between the π and d orbitals of the metallic nodes. Although the PCE of DSSCs fabricated with MOF-based or derived materials as the photoanodes is still relatively low, it is expected that the PCE of DSSCs can be improved through the development and use of electro-conductive MOFs and novel structured MOF photoanodes.

4.3. Utilization of MOFs and derivatives as counter electrodes in DSSCs

An important part of a DSSC is the counter electrode (CE), as it can catalyze the redox reactions of ion pairs and conduct electrons from an external circuit through the electrode into the electrolyte. Currently, platinum (Pt) has been widely used as a CE due to its high electrical conductivity and excellent electrocatalytic activity. However, the high cost, high scarcity and unsatisfactory long-term operation stability of Pt

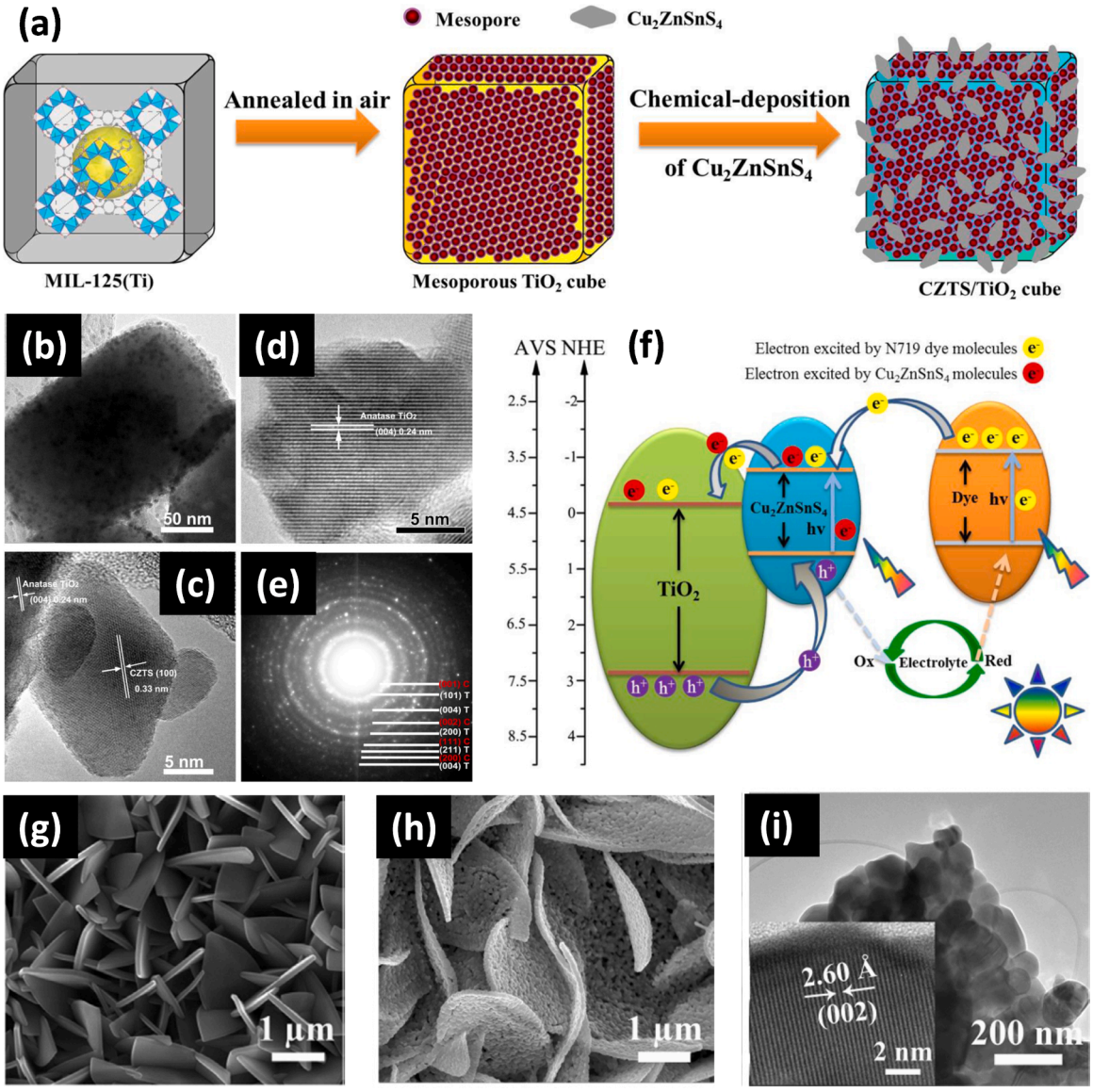

Fig. 4. (a) Schematic illustration of the two-step synthesis process of CZTS/TiO_2; (b-c) Low-magnification TEM image of CZTS/TiO_2 material; (d) HRTEM image of CZTS/TiO_2 material. The marked d-spacing shown in (c) and (d) is 0.24 and 0.33 nm, corresponding to the (004) plane of anatase TiO_2 and the (100) plane of CZTS, respectively. (e) Selected area electron diffraction pattern from the CZTS/TiO_2 heterostructure and (f) Schematic illustration of the energy band structure and photogenerated charge-transfer mechanism using CZTS/TiO_2 as a photoanode. Reproduced with permission [141]. Copyright 2016, American Chemical Society. (g) SEM image of top-view of the leaf-like-shaped ZIF-L crystals; (h) SEM image of top-view of ZnO nanosheet derived from ZIF-L and (i) TEM image of ZnO nanosheet. The inset HRTEM image shows the lattice structure of ZnO. Reproduced with permission [148]. Copyright 2014, Elsevier B.V.

Table 3
Performance of MOF-derived materials as photoanodes for DSSCs.

MOFs	MOF-derived photoanode	J_{sc} (mA cm^{-2})	V_{oc} (V)	FF	PCE (η, %)	PCE_{ref}, (η, %)	η/η_{ref}	Ref.
MIL-125 (Ti)	anatase TiO_2	13.99	0.768	0.67	7.20	$\eta_{P25} = 6.37$	1.13	[138]
MIL-125 (Ti)	hier-TiO_2/nc-TiO_2	19.1	0.66	0.55	7.1	$\eta_{nc\text{-}TiO2} = 4.6$	1.54	[139]
MIL-125 (Ti)	mesoporous TiO_2	16.51	0.74	0.61	7.45	$\eta_{TiO2} = 5.36$	1.39	[140]
MIL-125 (Ti)	Cn_2ZnSn_4/TiO_2	17.27	0.81	0.5818	8.10	$\eta_{TiO2} = 3.67$	2.21	[141]
MIL-125 (Ti)	MoS_2/dual-phase TiO_2	17.72	0.60	0.7788	8.96	$\eta_{TiO2} = 4.41$	2.03	[142]
$[Ni(bpp)(H_2O)_2]_3[P_2W_{18}O_{62}]\cdot 24\ H_2O$	P_2W_{18}·NiO@TiO_2	17.68	0.747	0.572	7.56	$\eta_{P25} = 5.98$	1.26	[143]
$H_6[Cu_3(H_2O)_6(P_2W_{18}O_{62})_2\cdot 3\text{-dpye})_6]\cdot 28\ H_2O$	P_2W_{18}·CuO@TiO_2	17.51	0.746	0.564	7.37	$\eta_{P25} = 5.98$	1.23	[143]
$[Zn(l\text{-}L_{Cl})(Cl)](H_2O)$ (MOF 1)	ZnO microparticles	N/A	N/A	N/A	0.15	N/A	N/A	[146]
$[Zn(l\text{-}L_{Br})(Br)](H_2O)$ (MOF 2)	ZnO microparticles	N/A	N/A	N/A	0.14	N/A	N/A	[146]
MOF-5	ZnO parallelepipeds	8.13	0.663	0.68	3.67	$\eta_{ref} = 3.15$	1.16	[147]
ZIF-L	ZnO nanosheets	6.87	0.565	0.649	2.52	$\eta_{ref} = 1.27$	1.98	[148]
ZIF-8	ZnO aggregates	9.13	0.667	0.554	3.37	N/A	N/A	[149]

in the electrolyte severely limits its large-scale use in DSSCs for practical applications. Therefore, it is highly desirable to develop CE without using noble metals. Interestingly in recent years, there has been a remarkable increase of reports focusing on the application of MOFs materials, particularly MOFs-derived materials as CEs in DSSCs.

4.3.1. MOFs as CE in DSSCs

A zirconium-based MOF-525 was first reported as electrocatalyst for the CE by Li et al. [150]. It was found that both its metal nodes, zirconium oxide, and pyrrole-based linker, (meso-tetra(4-carboxyphenyl) porphyrin), exhibited electrocatalytic activity for the reduction of I_3^- [150]. The counter electrode consisting of MOF-525 and sulfonated polythiophene binder exhibited a much higher PCE value of 8.91%, compared to that of 8.21% with a platinum CE. Further studies on an electrically conductive Cu-based MOF (Cu-MOF) as an electrocatalyst found its nature was due to the effective elevation of its heterogeneous rate constant instead of the increase in active surface area [151]. The Cu-MOF/poly(3,4-ethylenedioxythiophene) (Cu-MOF/PEDOT) composite electrode exhibited a superior electrocatalytic activity in multiple redox mediators, including I^-/I_3^-, cobalt(II/III)-complex, and copper (I/II)-complex. Such a high electrocatalytic performance could be due to the heterogeneous structure of the composite, enabling it to increase heterogeneous rate constant, increase the charge transfer and the penetration of the redox mediators, in addition to the exposure of more $(-Cu-S-)_n$ active sites.

ZIF (zeolitic imidazolate framework) is a specific type of MOF, and ZIF-8 has been studied as CE for DSSCs. It was mixed with the conductive binder polystyrenesulfonate-doped poly(3,4-ethylenedioxythiophene) (PEDOT:PSS) and applied as a CE in an iodine electrolyte and cobalt electrolyte respectively [152]. It was reported that the ZIF-8/PEDOT:PSS CE exhibited a superior electrocatalytic performance towards Co^{3+} reduction with PCE of 6.84%, but further investigation is required to analyze the nature of ZIF-8 electrocatalytic sites.

Apart from being used as the electrocatalyst in CE for DSSC, MOFs have also been investigated as a support or coordinator for the high dispersion of active sites in CE. Zhang et al. used a 2D layered MOF constructed from porphyrin ligand (5, 10, 15, 20)-tetra(4-carboxyphenyl)-porphyrin and zinc acetate (Zn-TCPP) as a support for electrocatalytic active single atomic Pt. The porphyrin struts in Zn-TCPP provide N-coordinating cavities to Pt ions and further disperse the metal active sites at the atomic level [153]. When the resulting Zn-TCPP-Pt was assembled as a CE in DSSC, it exhibited a competitive electrocatalytic performance compared to the commercial Pt, with a higher light transmission capacity under visible light. The important performance results and relevant parameters of MOF based materials as CE for DSSCs are summarized in Table 4.

4.3.2. MOF derivatives as CE in DSSCs

Compared to the pristine MOFs, MOF derivatives are more commonly used as CE in DSSCs due to the nature of the derivatives. Various types of electrocatalysts including metal carbides, metal nitrides, metal sulfides, metal selenides, and carbons have been widely studied as the CE materials in DSSCs. MOF derivatives including carbonaceous materials and transition metal compounds (TMCs) with hierarchical structures usually possess good electrical conductivity due to the in-situ formed carbons. They can be readily produced by using MOFs as a template/precursor [154–160]. However, pristine MOFs frequently exhibit low or poor electrical conductivity as their organic linkers are normally non-conductive. This results in MOF derivatives being more commonly used as CEs in DSSCs rather than pristine MOFs. Inspired by their intrinsic high surface areas, large pore volumes and diverse structures, MOFs have been extensively studied as novel templates/precursors for the preparation of various hierarchically structured materials. These MOF-derived materials possess the following unique advantages when used as a CE in DSSCs: (1) the chemical compositions are tuneable by choosing desired MOFs followed by specific thermal treatment; (2) the synthesized structures with controllable surface area and porosity can facilitate the access of electrolyte into the electrode; (3) the active components are atomically, homogenously dispersed onto high surface porous carbons formed in-situ.

4.3.2.1. ZIF-67 derivatives as CE. ZIF-67 is a sodalite-type porous structure assembled via chemical interactions between cobalt cations (as the metal source) and 2-methylimidazole (as the organic ligand), which frequently displays rhombic dodecahedral morphology. The uniformly distributed cobalt nodes in ZIF-67 ensures it can serve as an excellent cobalt source to synthesize cobalt-based compounds. Moreover, the nitrogen containing 2-methylimidazole ligand in ZIF-67 can be readily transformed into heteroatom-doped nanostructured carbon under high temperature heat treatment, which is beneficial for DSSCs. As metallic cobalt, cobalt oxides, cobalt sulfides, cobalt selenides and heteroatom-doped carbon materials are well-known Pt-free electrocatalysts to catalyze the reduction of triiodide ions. It is expected that these materials that are derived from ZIF-67 would be attractive materials as CE for DSSCs. So far ZIF-67 has been the most intensively studied MOF as a template/precursor for the construction of CE for DSSCs. ZIF-67 derivatives including metallic cobalt-based composites, cobalt sulfides, cobalt-molybdenum sulfides, cobalt selenides, and cobalt tellurides have been explored as CE for DSSCs [155, 161–179].

Metallic cobalt-based carbon nanocomposites. There are a few studies focused on the synthesis and CE performance of metallic cobalt-based carbon nanocomposites derived from ZIF-67 [155, 161–164]. Among them, three papers reported metallic cobalt nanoparticles embedded carbons derived from ZIF-67 as a CE for DSSC applications [161–163]. ZIF-67 powders were heated/carbonized at high temperatures either in a nitrogen atmosphere to obtain Co nanoparticles embedded N-doped carbon [161,162], or in argon/hydrogen atmosphere to obtain Co nanoparticles embedded N-doped carbon nanotubes (Co@NCNT) [163]. Fig. 5a shows the preparation process of Co@NCNT. The dodecahedral ZIF-67 crystals (Fig. 5b) were first synthesized, then uniform carbon nanotubes were grown on the surface of the remaining ZIF-67 skeleton with highly dispersed Co nanoparticles after pyrolysis at 800 °C under an argon/hydrogen atmosphere (Fig. 5c-d) [163]. Different ZIF-67 particle sizes and thermal pyrolysis temperatures were studied to optimize the electrocatalytic performance of I_3^- reduction in DSSCs. In addition, Hao et al. found that both Co and CoO could be formed during the one-step pyrolysis, and the synergistic effect between the Co and CoO is beneficial to the electrocatalytic performance in DSSCs [164]. In another study a Ni source was introduced during the synthesis of ZIF-67, to obtain CoNi alloy@carbon nanotubes embedded carbon nanocages (CoNi@CNTs-C) after pyrolysis at 900 °C under an argon atmosphere [155]. The CoNi alloy nanoparticles are the active components that

Table 4
Performance of MOF-based materials as CE for DSSCs.

MOF	CE Materials	J_{sc} (mA cm^{-2})	V_{oc} (V)	FF (%)	PCE (η, %)	PEC_{Pt}, (η, %)	η/η_{pt}	Electrolyte	Ref.
MOF-525	MOF-525/s-PT	16.14	0.80	70	8.91	8.21	1.085	I^-/I_3^-	[150]
Cu-MOF	Cu-MOF/PEDOT	16.36	0.777	65	8.26	7.67	1.077	I^-/I_3^-	[151]
ZIF-8	ZIF-8/PEDOT:PSS	8.85	0.858	65.71	7.02	7.24	0.970	I^-/I_3^-	[152]
ZIF-8	ZIF-8/PEDOT:PSS	11.46	0.852	70.00	6.84	7.56	0.905	Co^{2+}/Co^{3+}	[152]
Zn-TCPP	Zn-TCPP-Pt	12.95	0.69	61.39	5.48	5.10	1.074	I^-/I_3^-	[153]

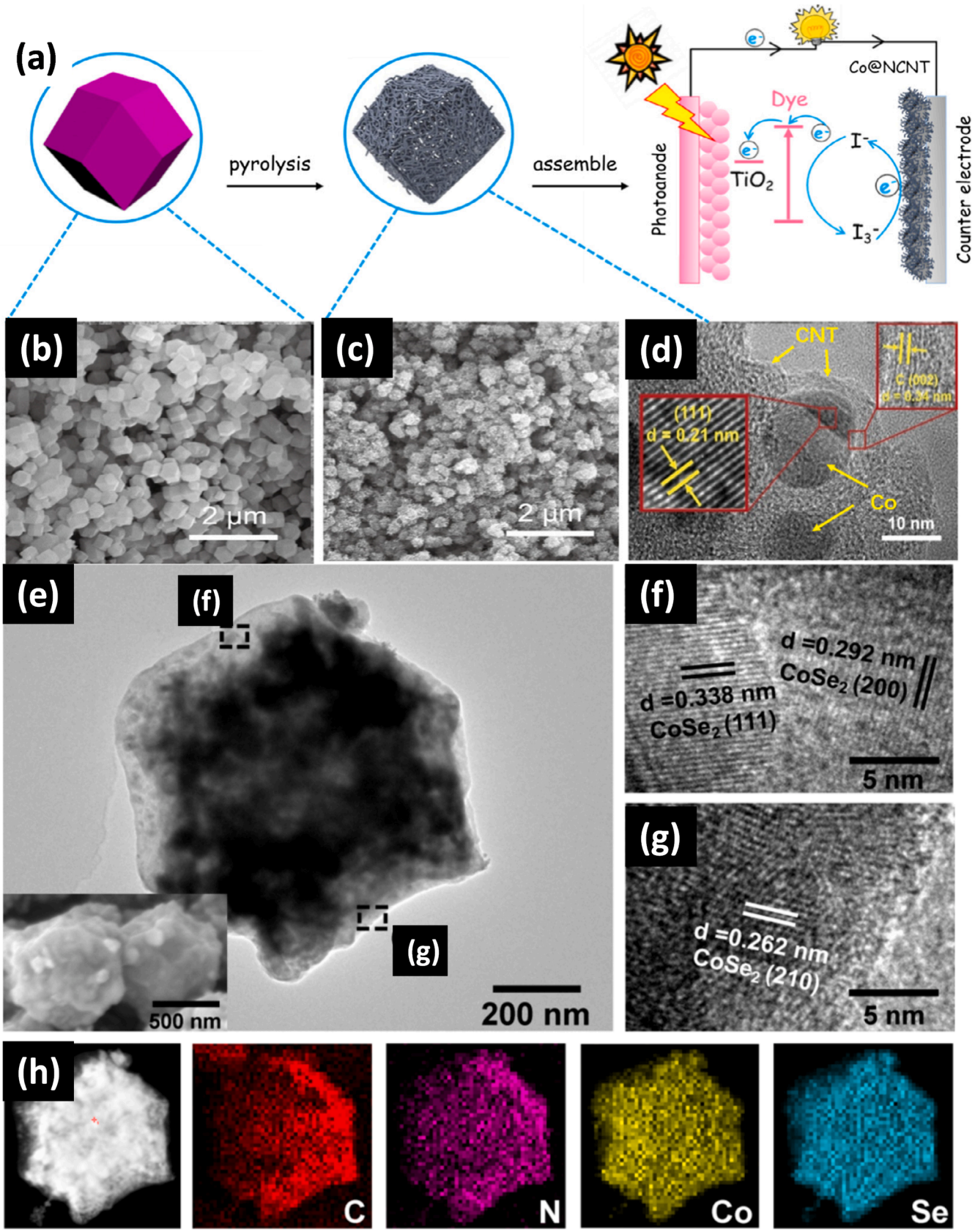

Fig. 5. (a) Schematic illustration of the fabrication process of Co@NCNT as a CE for DSSCs. (b) SEM image of ZIF-67. (c) SEM image and (d) TEM image of Co@NCNT-800. Reproduction with permission [163]. Copyright 2018, Elsevier B.V. (e) TEM and (f and g) HRTEM images of synthesized $CoSe_2$/NC. The inset in (e) is the SEM image of $CoSe_2$/NC. (h) Elemental mapping of $CoSe_2$/NC, C (red), N (purple), Co (yellow), and Se (blue). Reproduction with permission [167]. Copyright 2019, American Chemical Society.

catalyze the redox reactions, and the CNTs serve as a conductive network to prevent CoNi nanoparticles from aggregation and corrosion. When used as CE in DSSCs, the optimal CoNi@CNTs-C showed an impressive PCE of 9.04%, which is 15% higher than that of Pt-based cells (7.88%).

Cobalt sulfide-based materials. Cobalt sulfide-based materials are another important type of ZIF-67 derivatives used as CEs for DSSCs [165–170]. In 2014, Wu et al. prepared CoS nanoparticles with different sizes by oxidization and sulfurization of ZIF-67, and the resulting CoS nanoparticles were then coated onto FTO and used as a CE in DSSCs [165]. The CE with a small CoS nanoparticle size showed a PCE value of 8.1%, comparable to the Pt based DSSC (8.0%). In another example, CoS_2 nanoparticles embedded carbon were synthesized by sulfurization of ZIF-67 and showed a remarkable photoelectric conversion efficiency of 8.74%, which was mainly attributed to the synergic effect between CoS_2 and the in-situ formed carbon [167]. Moreover, a Co_3S_4 polyhedral loaded MoS_2 nanosheet composite (MoS_2 @Co_3S_4) in which MoS_2 was evenly distributed on the surface of hollow Co_3S_4 polyhedrons, was prepared by a hydrothermal method using ZIF-67 as a template/precursor/carrier [168]. When such a bimetallic sulfide structure is used as a DSSC CE, it is expected to increase the surface area, expose more catalytic active sites of MoS_2 and facilitate the diffusion and transfer of redox couples with a power conversion efficiency of 7.86%. Another example is Co_8FeS_8/N-C dodecahedral nanocages (DNCs), which were synthesized by a two-step sulfidation and cation exchange method using ZIF-67 as a template [169]. The fabricated DSSC using Co_8FeS_8/N-C as CE could achieve a PCE of 8.06%, which was higher than those of Pt and monometallic sulfide. This method may provide a new route to prepare bimetallic sulfides as a CE for DSSCs. In addition, Liu et al. prepared a complex W-N/C@Co_9S_8 @WS_2-hollow carbon nanocage using ZIF-67 as a template/precursor [170], attempting to create a multi-composition material that can achieve multifunctional electrocatalytic performance. The produced material exhibited a PCE of 7.38%, which was higher than that of Pt.

Cobalt-molybdenum sulfide-based materials. Hou's group extensively investigated ZIF-67 derived cobalt-molybdenum sulfide based materials as CEs for DSSCs [171–173]. They first prepared cobalt-incorporated molybdenum sulfide hollow nanoboxes (Co-MoS_x NBs) through a one-step template-engaged synthesis of raw material cube-shaped ZIF-67 and $(NH_4)_2MoS_4$ [171]. Due to the advantageous morphology of Co-MoS_x NBs, the as-prepared Co-MoS_x NBs as CE in DSSC showed a PCE value of 9.64%, which was higher than that of Pt (8.39%). Later, they designed a double-shelled hollow structured $CoMoS_x$ @Ni-$CoMoS_x$ hollow polyhedron catalyst using ZIF-67 as an initial template and cobalt source [172]. It was claimed that such a structure could not only provide more active sites of the catalyst, but also have more contact region for the reaction between the electrolyte and the catalyst. Another example of a structure designed from ZIF-67 is yolk-shell structured CoS_2/N-doped C@Co-WS_2 (CoS_2/NC@Co-WS_2) [173]. The synthesis process includes three stages: In Stage I, WS_4^{2-} from $(NH_4)_2WS_4$ and Co^{2+} from ZIF-67 first combined to form a Co-WS_x layer. In Stage II, the Co-WS_x consistently grew on the outer shell, forming the yolk-shell ZIF-67 @Co-WS_x. In Stage III, yolk-shell structured CoS_2/NC@Co-WS_2 was finally formed after an annealing process. This core-shelled structure was believed to provide a larger surface area, and more efficient active sites [180–182], thereby the CoS_2/NC@Co-WS_2 exhibited a superior PCE of 9.21%, which was much higher than that of Pt.

Cobalt selenide-based materials. Cobalt selenide-based materials derived from ZIF-67 have also been reported for application as a CE in DSSCs [167, 174–178]. $CoSe_2$ embedded in a N-doped carbon nanocage on the support of carbon cloth ($CoSe_2$/N-C@CC) was synthesized via a ZIF-67 growth-carbonization-selenization process [174] and applied as a CE for DSSCs, which exhibited a PCE value of 8.40%, higher than that of Pt based DSSCs (8.09%). Similarly, Wu et al. prepared hollow $CoSe_2$ nanoparticles embedded nitrogen-doped porous carbon anchored on nitrogen-doped carbon nanotubes ($CoSe_2$ @NPC/NCNTs). They used ZIF-67 combined with polypyrrole (PPy) as a template/precursor followed by a carbonization-selenization processing method [175]. They also prepared $CoSe_2$ particles confined in N-doped porous carbon interconnected by carbon nanotubes with internally encapsulated $CoSe_2$ ($CoSe_2$ @NPC/$CoSe_2$ @CNTs) by an in situ pyrolysis and selenization process. ZIF-67 was functioned as the template, precursor, and carbon source for the formation of CNTs [176]. Fu et al. reported a direct selenization of ZIF-67 process to prepare $CoSe_2$/N-doped carbon ($CoSe_2$/NC) with a rhombic dodecahedral morphology (Fig. 5e) [167]. Its structure was identified by HRTEM (Fig. 5f-g) and elemental mappings (Fig. 5h). The $CoSe_2$/NC based DSSC exhibited a satisfactory power conversion efficiency of 9.06%, which could be attributed to the synergic effect between $CoSe_2$ and NC. Recently, yolk-shell and core-shell structures have been proposed to design cobalt selenide-based materials derived from ZIF-67 [177,178]. Such structures are believed not only to increase the surface area, providing numerous active sites, but also to increase the interaction between the active sites and electrolyte, improving the absorbance and transfer of iodine ions. Consequently, their use as CEs in DSSCs resulted in an enhanced power conversion efficiency.

Cobalt telluride-based materials. Hou et al. synthesized $CoTe_2$ nanoparticles embedded in N-doped carbon nanotube-grafted polyhedrons ($CoTe_2$@NCNTs) using ZIF-67 as a template/precursor [179]. The assembled $CoTe_2$@NCNTs based DSSC exhibited an improved PCE of 9.02%, mainly due to the excellent electronical conductivity and high surface area of the N-doped CNTs, as well as the synergistic effect between $CoTe_2$ and CNTs.

4.3.2.2. ZIF-8 derivatives as CE. Like ZIF-67, ZIF-8 consists of zinc cations as the metal source and 2-methylimidazole as organic ligands, and it has also been studied as a precursor to generate derivatives for use as CEs in DSSCs. Wei et al. obtained porous carbonaceous material by direct carbonization of ZIF-8 under an inert atmosphere, followed by acid washing [183]. The carbon material obtained was applied as a CE and showed a performance ($\eta = 7.32\%$), comparable to that of Pt ($\eta = 7.53\%$). N-doped carbon sheet was later synthesized by carbonization of ZIF-8 integrated in graphene oxide [184]. The as-prepared N-doped carbon sheet was then assembled as a counter electrode into DSSCs for evaluation of photovoltaic performance, and an illustration of the assembled device is shown in Fig. 6a. The simulated solar irradiation performance of the reference sample, as-prepared N-doped carbon sheet, and the benchmark Pt was then carried out. A higher power conversion efficiency of 8.2% was achieved for the as-prepared N-doped carbon sheet, compared to the PCE of 7.6% for Pt, the corresponding parameters were deduced from Fig. 6b [184]. The group of Sung et al. considered the limitation of mass transfer resistance of I^-/I_3^- electrolytes in ZIF-8-derived carbon materials, and tried to increase the pore size of carbon by coating the surface of ZIF-8 with a layer of polydopamine before carbonization [185]. Such a polydopamine layer was claimed to promote an increase in the pore size (i.e. mesopore) of the resulting carbon material, which further improved the electrocatalytic reduction of triiodide on the surface of CE (shown in Fig. 6c). As a result, the as-prepared carbon material (ZIF-8-dopa-C) led to a PCE of 9.03%, superior to that of Pt [185].

Zhao's group prepared three different types of ZIF-8 derivatives: ZnO-nitrogen doped carbon (ZnO-NC) [186], m-SiO_2@nitrogen doped carbon [187], and MoS_2 grown on the nitrogen-doped carbon [188]. These materials were then each blended with Poly(3, 4-ethylenedioxythiophene poly styrene sulfonic acid (PEDOT: PSS) as CE. Electrochemical studies confirmed that when these as-prepared materials were used as counter electrodes in DSSCs, they exhibited catalytic activities superior to traditional Pt in both I^-/I_3^- based electrode and $[Co(bpy)_3]^{2+/3+}$ redox mediator [186–188]. As an example, 7% ZnO-NC/PEDOT:PSS CE exhibited a higher electron transfer ability at the CE/electrolyte interface, based on the Nyquist plots shown in

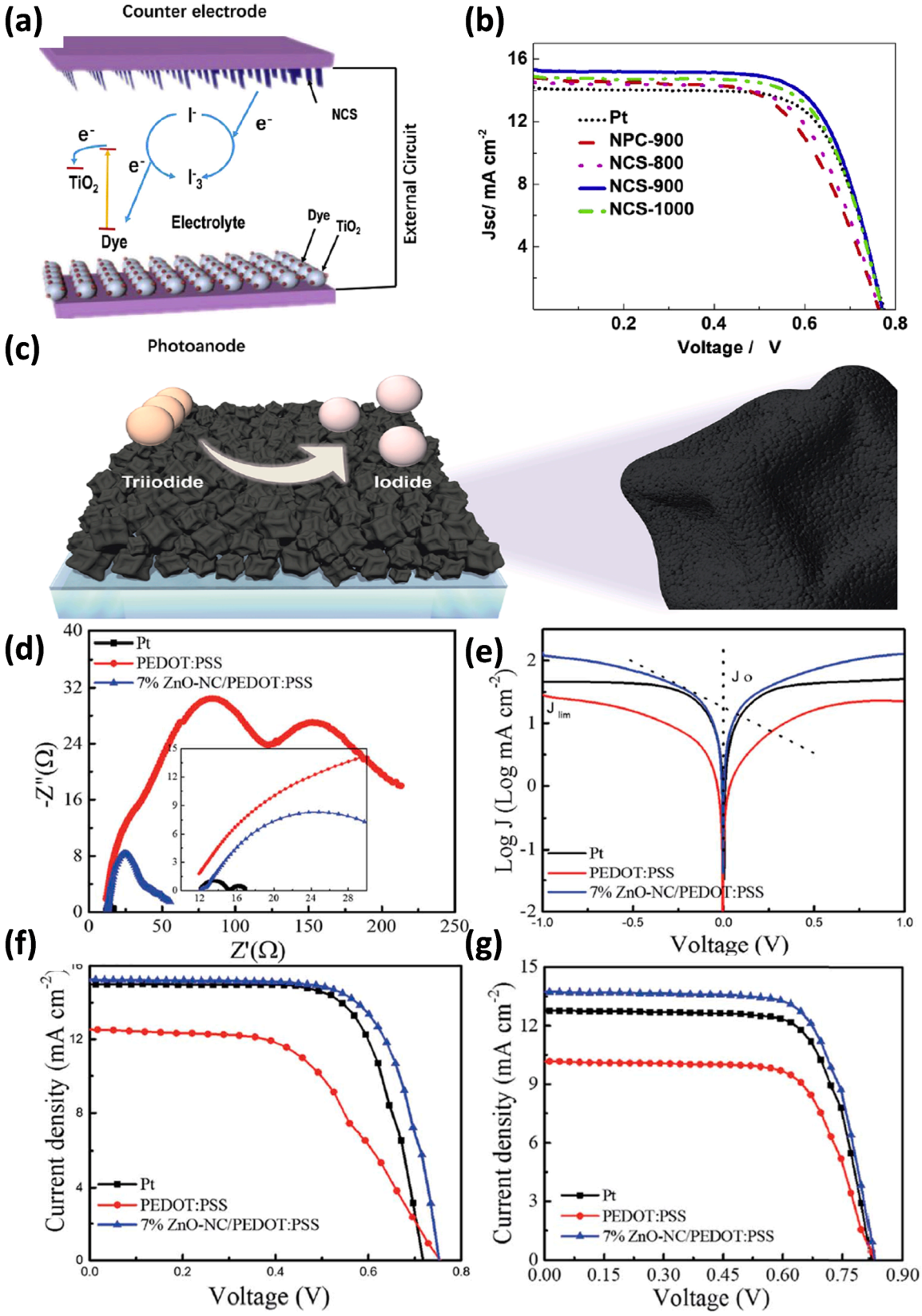

Fig. 6. (a) Schematic illustration of a DSSC assembled with N-doped carbon sheet derived from ZIF-8 as the CEs, and (b) the corresponding photocurrent density (J) vs. the photo voltage (V) curves of DSSC. Reproduced with permission [184]. Copyright 2018, Elsevier B.V. (c) Schematic illustration of the electrocatalytic reduction of triiodide at the surface of a mesoporous ZIF-8-doped-C CE. Reproduced with permission [185]. Copyright 2018, Royal Society of Chemistry. (d) The Nyquist plots, (e) Tafel polarization curves, and (f) J–V curves of the DSSCs using Pt, reference sample PEDOT:PSS, and ZnO-NC/PEDOT:PSS CE in I_3/I^- redox couple system. (g) J–V curves of the DSSCs using reference sample Pt, PEDOT:PSS, and ZnO-NC/PEDOT:PSS CE in $[Co(bpy)_3]^{2+/3+}$ redox couple system. Reproduced with permission [186]. Copyright 2019, American Chemical Society.

Fig. 6d. Moreover, this 7% ZnO-NC/PEDOT:PSS CE also showed a superior exchange current density (J_0), as its Tafel slope was greater than that of the reference PEDOT:PSS CE, and even close to that of the Pt (Fig. 6e). As a result, the 7% ZnO-NC/PEDOT:PSS CE based DSSC reached a PCE of 8.05%, which is close to the Pt-based device (η_{Pt} = 8.51%) in the I_3^-/I^- redox couple system (Fig. 6f). In addition, in the [Co(bpy)$_3$]$^{2+/3+}$ redox couple system, shown in Figs. 6g, 7% ZnO-NC/PEDOT:PSS CE also exhibited a greater electrocatalytic performance toward the [Co(bpy)$_3$]$^{2+/3+}$ reduction reaction, with a high PCE of 8.12% [186].

Rather than using ZIF-8 for the synthesis of carbon materials, Wang et al. instead sulfurized ZIF-8 to obtain ZnS micropolyhedrons [189], which showed excellent performance as CE in DSSCs for electrocatalytic reduction of I^-/I_3^- due to the ZIF-8 skeleton.

4.3.2.3. Other MOF derivatives as CE. Apart from ZIF-67 and ZIF-8, other types of MOFs including Prussian blue analogue ($Co_3[Co(CN)_6]_2$) [190], Co-MOF [191], Ni-MOF (NiBDC) [192], ZIF-7 [193], Ni–Co-MOF [194], cobalt−metalloporphyin MOF (PIZA-1) [195], and Cu-TCPP MOF [196], have been studied as precursors to explore their derivatives as counter electrodes in DSSCs. Their corresponding derivatives including CoS_x, $CoSe_2$, bimodal mesoporous carbon with embedded Ni nanoparticles (BMCNi), ZnSe/N-doped carbon, $NiCo_{0.2}$@C, $CoS_{1.097}$@N-doped carbon, and $Cu_{2-x}Se$@N-doped carbon, respectively, were applied as CEs for DSSCs, with all exhibiting electrocatalytic performance comparable to that of Pt-based DSSCs. Details of these results are presented in Table 5. The use of other types of MOFs as a template/precursor provides a new approach for rational design of electrocatalysts with desired compositions.

4.3.3. Summary

Although MOFs possess periodic intra-framework functionality that enables them to form high density and well distributed catalytically active sites, most pristine MOFs are electrically insulating, which limits their electrocatalytic performance as CEs for DSSCs. Therefore, the design of new types of electrically conductive MOFs or the formation of MOF composites containing MOFs and conducting polymers is a promising route to improve the electrocatalytic performance [54,198].

Compared to pristine MOFs, their derivatives are more common as CEs in DSSCs. The cell efficiency and other important parameters of DSSCs assembled with MOF-derivatives as CEs in comparison with the DSSCs fabricated with Pt are summarized in Table 5. So far, most of the studies are focused on ZIF-67 and ZIF-8 based derivatives, and studies on other types of MOF derivatives are rare. In general, as listed in Table 5, the DSSCs fabricated with MOF-derivatives as CEs can achieve comparable or even higher PCE values compared to those fabricated with Pt as a CE. Recent studies have focused mainly on the design of multi-component active sites with hierarchical complex structures, attempting to make use of the fact that two or more active sites may have a synergistic effect to further enhance the electrocatalytic activity. Moreover, the hierarchical complex structures such as hollow, core-shell, and yolk-shell structures can provide more active sites and increase the contact between electrode and electrolytes, as well as improve the electrode stability. Given the diversity of MOFs, the emergence of more studies on the design and preparation of hierarchical complex structures for applications as CEs in DSSCs with high PCE is expected.

4.4. Utilization of MOFs as electrolytes in DSSCs

The poor long-term durability of DSSCs is one of the main factors that hamper their practical use. The risk of liquid electrolyte leaking, and the volatilization of the organic solvents are factors that contribute to low durability in DSSCs. Due to the inorganic-organic feature, high porosity and rich functionality, MOFs show great potential to modify or replace the traditional liquid organic solvents used in DSSCs.

MOFs can be used as an additive in the electrolytes of DSSCs. In 2013, Bella et al. [199] first reported a MOF-polymer electrolyte membrane for quasi-solid DSSCs with solar energy conversion efficiencies of 4.8% and high-stability. In this study a Mg-based MOF (Mg-MOF) was dispersed in a UV-curable reactive polymer mixture prepared by mixing poly(ethylene glycol) methyl ether methacrylate (PEGMA) and polyethylene glycol diacrylate (PEGDA). After a rapid UV-induced curing, the MOF-polymer membrane was prepared. It is claimed that the interactions between the organic shell of the Mg-MOF crystals and the surface groups of the TiO_2 layer were the main factors

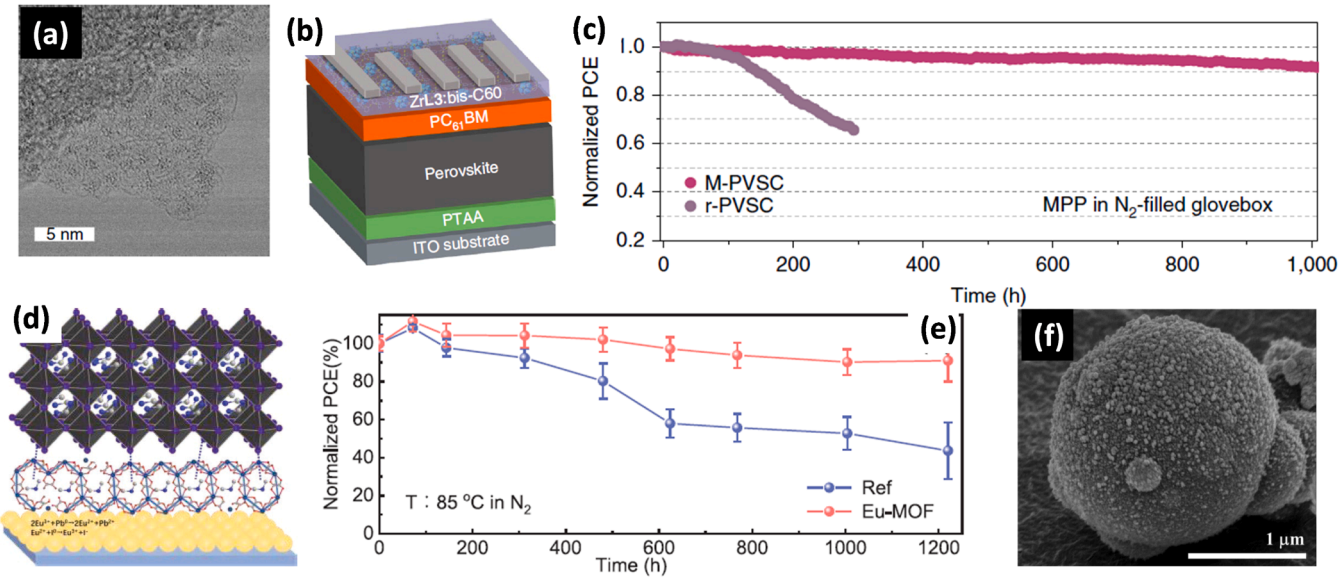

Fig. 7. (a) TEM image of 2D MOF ZrL3; (b) Device structure of inverted PSC with ZrL3:bis-C60 electron-extraction layer; (c) Long-term stability performance of ZrL3 based PSC under maximum power point of 1.03 V recorded at 85 °C under continuous light irradiation in a N_2-filled glovebox for 1000 h. Reproduced with permission [208]. Copyright 2020, Spring Nature. (d) Schematic illustration of the Eu-MOF layer on a perovskite film; and (e) Long-term stability performance of Eu-MOF based PSC upon continuous heating at 85 °C in N_2 for 1200 h. Reproduced with permission [209]. Copyright 2021, John Wiley & Sons. (f) SEM image of a NiO@C particle derived from MOF Ni-BTC. Reproduced with permission [210]. Copyright 2020, Elsevier B.V.

Table 5
Performance of MOF derivatives as CE for DSSCs.

MOFs	MOF-derived counter electrode	J_{sc} (mA cm^{-2})	V_{oc} (V)	FF	PCE (η, %)	PEC_{Pt}, (η, %)	η/η_{pt}	Electrolyte	Ref.
ZIF-67	CoS	14.7	0.784	0.71	8.1	8.0	1.013	I^-/I_3^-	[165]
ZIF-67	Co-MoS_x	17.4	0.804	0.687	9.64	8.39	1.149	I^-/I_3^-	[171]
ZIF-67	Co embedded carbon	21.44	0.730	0.680	10.6	9.8	1.082	I^-/I_3^-	[162]
ZIF-67	CoS_2 embedded carbon	16.9	0.73	0.66	8.20	7.88	1.041	I^-/I_3^-	[166]
ZIF-67	Co/N-doped carbon	16.86	0.75	0.62	7.84	7.40	1.059	I^-/I_3^-	[161]
ZIF-67	$CoSe_2$/N-doped carbon	18.86	0.72	0.67	9.06	8.03	1.128	I^-/I_3^-	[167]
ZIF-67	CoS_2/N-doped carbon	18.51	0.724	0.65	8.74	8.03	1.088	I^-/I_3^-	[167]
ZIF-67	Co_8FeS_8/ N-doped C	18.19	0.75	0.58	8.06	7.35	1.097	I^-/I_3^-	[169]
ZIF-67	Co_3O_4-WC-CN/rGO	16.27	0.77	0.59	7.38	6.85	1.077	I^-/I_3^-	[197]
ZIF-67	$CoTe_2$@NCNTs	17.89	0.787	0.64	9.02	8.03	1.123	I^-/I_3^-	[179]
ZIF-67	MoS_2@Co_3S_4	16.21	0.782	0.62	7.86	6.99	1.124	I^-/I_3^-	[168]
ZIF-67	CoNi@CNTs-C	18.3	0.76	0.65	9.04	7.88	1.147	I^-/I_3^-	[155]
ZIF-67	CoS_2/NC@Co-WS_2	16.5	0.815	0.670	9.21	8.18	1.126	I^-/I_3^-	[173]
ZIF-67	Co/CoO-Co@NGC	13.29	0.80	0.74	7.92	8.18	0.968	I^-/I_3^-	[164]
ZIF-67	Co@N-doped CNT	15.87	0.72	0.711	8.18	7.54	1.085	I^-/I_3^-	[163]
ZIF-67	$CoSe_2$/N-C@CC	16.39	0.730	0.702	8.40	8.09	1.038	I^-/I_3^-	[174]
ZIF-67	$CoMoS_x$ @Ni-$CoMoS_x$	18.4	0.789	0.641	9.30	8.01	1.161	I^-/I_3^-	[172]
ZIF-67	Ni-$MoSe_x$ @$CoSe_2$ CSNs	17.3	0.815	0.683	9.58	8.32	1.151	I^-/I_3^-	[178]
ZIF-67	$CoSe_2$-NC@Co-$FeSe_2$	17.9	0.806	0.667	9.61	8.15	1.179	I^-/I_3^-	[177]
ZIF-67	CoS_2-NC@Co-FeS_2	17.2	0.805	0.663	9.18	8.15	1.126	I^-/I_3^-	[177]
ZIF-67	CoSe@NPC/NCNTs	16.00	0.710	0.67	7.58	7.27	1.043	I^-/I_3^-	[175]
ZIF-67	CoSe@NPC/CoSe@CNTs	15.90	0.701	0.66	7.36	7.16	1.028	I^-/I_3^-	[176]
ZIF-67	W-N/C@Co_9S_8@WS_2	15.74	0.72	0.65	7.39	7.06	1.047	I^-/I_3^-	[170]
ZIF-8	ZnS	17.20	0.711	0.67	8.20	8.24	0.995	I^-/I_3^-	[189]
ZIF-8	ZnO-C	13.56	0.77	0.68	7.32	7.53	0.972	I^-/I_3^-	[183]
ZIF-8	N-doped carbon	15.29	0.811	0.728	9.03	8.85	1.020	I^-/I_3^-	[185]
ZIF-8	N-doped carbon	15.25	0.77	0.6986	8.2	7.6	1.079	I^-/I_3^-	[184]
ZIF-8	m-SiO_2@NC-PEDOT:PSS	18.88	0.76	0.6979	10.01	8.50	1.178	I^-/I_3^-	[187]
ZIF-8	ZnO-NC/PEDOT:PSS	15.20	0.74	0.7088	8.05	8.51	0.946	I^-/I_3^-	[186]
ZIF-8	ZnO-NC/PEDOT:PSS	13.58	0.836	0.7149	8.12	7.49	1.084	Co^{2+}/Co^{3+}	[186]
ZIF-8	MoS_2/NC-PEDOT:PSS	14.69	0.75	0.6932	7.67	7.86	0.976	I^-/I_3^-	[188]
ZIF-8	MoS_2/NC-PEDOT:PSS	13.36	0.857	0.7121	7.87	7.49	1.051	Co^{2+}/Co^{3+}	[188]
$Co_3[Co(CN)_6]_2$	CoS_x	16.8	0.73	0.70	8.48	8.01	1.059	I^-/I_3^-	[190]
Co-MOF	$CoSe_2$	16.26	0.68	0.62	6.86	6.36	1.079	I^-/I_3^-	[191]
NiBDC	BMCNi	16.73	0.739	0.694	8.6	8.4	1.024	I^-/I_3^-	[192]
ZIF-7	ZnSe/N-doped carbon	16.40	0.77	0.69	8.69	8.26	1.052	I^-/I_3^-	[193]
Ni–Co-MOF	$NiCo_{0.2}$@C	17.80	0.780	0.67	9.30	8.04	1.157	I^-/I_3^-	[194]
PIZA-1	$CoS_{1.097}$@N-doped C	17.26	0.76	69.42	9.11	8.04	1.133	I^-/I_3^-	[195]
Cu-TCPP	$Cu_{2-x}Se$@N-doped C	13.12	0.89	0.6544	7.61	8.46	0.900	Co^{2+}/Co^{3+}	[196]

responsible for the enhanced PCE of DSSCs.

Due to the highly porous and sponge-like characteristics, MOFs can hold a large amount of liquid electrolyte, while still maintaining the electrolyte system [21,200]. MOF gel-based electrolyte is another attempt for the utilization of MOFs as an electrolyte for DSSCs. Recently, Han et al. reported the gelation of Al-MOF as an electrolyte for DSSC [200]. Al-MOF consisting of Al^{3+} and 1,3,5-benzenetricarboxylate (H_3BTC), was first mixed with a conventional liquid electrolyte. This MOF-containing electrolyte was then injected into the DSSC to introduce gelation within the cells, so that the electrolyte could penetrate evenly into the pores of TiO_2, achieving a good interfacial contact. Like this study, Su et al. used this gelation method to prepare two types of metal–organic gel (MOGs) based electrolyte for efficient quasi-solid-state DSSCs [201,202]. One MOG was assembled by Al^{3+} and H_3BTC [201], and the other by Al^{3+} and 4-tert-butylpyridine (TBP) [202]. As-assembled gel electrolytes can hold a considerable number of active species of the electrolyte, thereby largely preserving the properties of the liquid electrolyte.

In summary, the studies on the use of MOFs as electrolytes for DSSCs are currently in the early stages. The formation of MOF-polymer and MOF-based gels are two popular electrolyte materials for DSSCs reported in the literature. Further work in this area focused on the design and optimization of new MOF-polymers, and the functionality of the MOF-based gels as electrolytes. This is directing research towards a durable and efficient DSSC using an easy-preparation and cost-effective approach which is highly desirable.

5. Applications in perovskite solar cells

Perovskite materials with prominent optoelectronic properties including a long exciton diffusion length, ambipolar charge-transporting ability, intense and wide-range light absorption, low-cost, solution processable are the main characteristics of photoactive materials in perovskite solar cells (PSCs). MOF-based materials, including both pristine MOFs and MOF derivatives, have been widely explored as functional materials for use in PSCs not only as an interfacial layer, electron transport layer (ETL) or hole transport layer (HEL), but also as additives in the heterojunction perovskite layer.

The functional materials used in PSCs are required to simultaneously possess: 1) optimal energy level alignment including HOMO and Fermi levels (E_f) considered to minimise the energy lost [203]; 2) high charge selectivity to promote charge extraction and to avoid charge accumulation that blocks carriers; 3) sufficient conductivity to avoid resistive losses; 4) optimal transparency to limit optical losses; 5) ease of processing; and 6) stability under working conditions [89]. The recent progress in the utilization of MOF-based and derived materials in PSCs is discussed in this part.

5.1. Utilization of MOFs and derivatives as interfacial layer in PSCs

There are few reports which have demonstrated the utilization of MOFs and their derivatives as interfacial layers (interlayer) in PSCs. Three types of MOFs including ZIF-8 [204–207], a 2D conjugated MOF (Zr**L3**) [208], and Eu-MOF [209] were studied, while only one MOF derivative NiO@C was applied as an interfacial layer for PSC [210].

These MOFs and derivatives are anticipated to enhance the perovskite crystallinity and grain size, thus further improving the photovoltaic performance of PSCs.

5.1.1. MOFs as interfacial layer in PSCs

Due to its chemical robustness, good thermal stability and ability to grow on many types of substrate, ZIF-8 has drawn wide attention as an interfacial layer for PSCs. In 2018, Wei et al. first applied a ZIF-8 interfacial layer between the mp-TiO_2 and perovskite layer in a PSC. This ZIF-8 interfacial layer improved the perovskite layers crystallinity and morphology. The photovoltaic performance of the ZIF-8 modified conventional n–i–p PSC was enhanced to a PCE of 16.99%, due to the suppression of photo-generated carrier recombination and the improvement of charge extraction [204]. Similarly, Wang et al. and Eslamian et al. independently introduced a ZIF-8 interfacial layer between the TiO_2 and perovskite layer in PSCs [205,206]. Wang et al. demonstrated that the ZIF-8 interlayer could absorb additional light in the short-wavelength range above 350 nm, and facilitate the speed of excited electron transfer [205]; while Eslamian et al. synthesized a ZIF-8 interlayer at room temperature as a scaffold to improve the perovskite grain crystallinity [206]. In addition, Zhang et al. synthesized ammonium salt-trapped ZIF-8 capsules (ZIF-8 @FAI) as an interlayer between the perovskite layer and the hole transport layer (HTL) [207]. This ZIF-8 @FAI layer improved the conventional n–i–p PSC device efficiency (i.e. PCE = 19.13%) and enhanced its stability which remained over 93% of its initial efficiency after 150 h of operation.

As the stability of PSCs is currently still a challenge, Jen et al. reported the use of a thiol-functionalized 2D conjugated MOF (Zr**L3**) (shown in Fig. 7a) to address this issue [208]. The Zr**L3** functioned as an electron-extraction layer between the perovskite and the cathode (shown in Fig. 7b). The Zr**L3** integrated n–i–p PSC showed a high PCE value of > 22%, with a certificated value of 21.3%. In terms of the stability, the fabricated PSC could remain > 90% of its initial efficiency under continuous light irradiation (maximum power point) for 1000 h at 85 °C (Fig. 7c). In addition, the Zr**L3** layer could also capture lead ions leaked from the PSC [208]. Recently, Chen's group introduced an ultrathin Eu-MOF layer at the electron transport layer (ETL)/perovskite absorber interface to improve the PCE and stability of the planar PSC with a typical n-i-p configuration (Fig. 7d) [209]. The incorporation of the Eu-MOF layer brings several benefits including: (1) the increase in light adsorption; (2) the conversion of residual tensile strain into compressive strain in the perovskite film and (3) the passivation of the perovskite film to form high-quality crystals. Due to the synergetic effects described, the Eu-MOF incorporated PSC achieved a high PCE of 22.16%, as well as excellent stability, where the PSC could remain at 96% of its initial efficiency after 2000 h in a relative humidity of 30% and 91% of the initial efficiency after 1200 h continuous aging in N_2 at 85 °C (Fig. 7e) [209].

5.1.2. MOF derivatives as the interfacial layer in PSCs

The research on the use of MOF derivatives as an interfacial layer in PSCs is at its infancy and only one report is currently available. Bark et al. reported the synthesis of NiO@C nanoparticles by thermolysis of a Ni-MOF, Ni-benzene-1,3,5-tricarboxylic acid (Ni-BTC), in air at 400 °C. [210] As shown in Fig. 7f, the morphology of the NiO@C particle is spherical with a rough surface. The as-prepared NiO@C thin film was then applied as an interfacial layer inserted between the perovskite layer and hole-transfer layer (HTL) (i.e. spiro-OMeTAD) in PSC. The NiO@C thin film showed high porosity and improved electro-conductibility, leading to fewer perovskite defects and a greater charge transfer efficiency. As a result, the NiO@C integrated PSC with a regular n-i-p configuration exhibited an enhanced PCE of 15.78%, which was higher than that of the reference without using NiO@C (13.79%) [210].

5.2. Utilization of MOFs and derivatives as electron transport layer in PSCs

Two Ti-based MOFs MIL-125 (Ti) and NH_2-MIL-125 (Ti), as well as NH_2-MIL-101 (Fe) have been synthesized and processed into films for utilization as electron transport layers (ETL) in PSCs [211,212]. The fabrication method of the MOF film plays an important role for the quality of ETL, which largely determines whether an efficient and low-cost PSC is achievable. In terms of MOF derivatives, TiO_2 derived from MIL-125 (Ti), Co-doped Ti-BTC as well as NH_2-MIL-125 (Ti), and ZnO derived from ZIF-8 are the two main materials that have been explored as ETL in PSC [87, 88, 213–216].

5.2.1. MOFs as ETL in PSCs

Ti-based MOFs are ideal candidates as ETL in PSCs, mainly due to their well-ordered structures consisting of tailorable Ti oxo-clusters and organic ligands [217]. Choi et al. designed and prepared a flexible PSC using nanocrystalline MIL-125 (Ti) film at room temperature as an ETL in combination with [6,6]-phenyl-C_{61}-butyric acid (PCBM) [211]. Fig. 8a shows a schematic illustration of the synthesis process for MIL-125 (Ti). The advantage of using MIL-125 (Ti) is that its nanocrystalline form can enhance the film uniformity of the ETL, which increases the compatibility of the Ti-MOF with the perovskite materials due to its solution processability. The assembled PSC device follows the conventional n − i − p planar heterojunction structure (shown in Fig. 8b). The as-prepared ETL can not only provide efficient electron transfer, but also suppress the contact between the perovskite layer and electrode, resulting in a high PCE of 17.43% and excellent mechanical stability [211]. Similarly, Perez et al. synthesized two types of MOFs NH_2-MIL-101 (Fe) and NH_2-MIL-125 (Ti), and then applied them as ETLs in PSCs with a n-i-p type structure using spin coating and liquid epitaxy methods [212]. The thickness of the ETL was optimized to achieve reasonable power conversion efficiencies. While NH_2-MIL-101 (Fe) based PSC exhibited a PCE of 4.1%, and NH_2-MIL-125 (Ti) based PSC showed a higher PCE of 5.9%. It was found that the morphology of the MOF films, including porous nature and surface roughness, could greatly affect the overall performance of the PSCs [212].

In summary, so far only very limited studies on MOFs as ETL in PSCs have been reported. These studies show that the uniformity and surface morphology of MOF-based ETL play important roles in the performance of PSCs. Therefore, further studies on morphology control of MOFs for enhanced performance of PSCs are in demand. In addition, spin coating was applied in reported studies, and other potential solution-based thin film fabrication technologies such as spray coating and roll-to-roll coating, could be investigated in the future to achieve efficient and flexible PSCs.

5.2.2. MOF derivatives as ETL in PSCs

TiO_2 is one of the main MOF derivatives that have been studied for PSCs. In spite of that TiO_2 derived from MIL-125 (Ti) acts as a nanostructure scaffold with scattered distribution, helping to improve the quality of the perovskite film with increased crystallinity and reduced pin-holes [213], most TiO_2 derived from MOFs are studied as ETL in PSCs [87,88,214]. For example, Bark et al. prepared porous Co-doped TiO_2 by thermal decomposition of Co-doped Ti-BTC at 400 °C in air [214], which reduces the TiO_2 band gap and improves the electron transfer. When applied as an ETL, 1 wt% Co-doped TiO_2 integrated PSCs with a n-i-p type structure exhibited an optimal PCE of 15.75%, which was higher than that of the PSC using commercial TiO_2 (14.42%) [214]. Liu et al. prepared porous anatase TiO_2 nanocrystals derived from MIL-125 (Ti), and used them in the carbon-based n-i-p PSC by screen-printing [87]. The as-prepared TiO_2 nanocrystals with cake-like structure was beneficial to the crystallization of perovskite materials, as well as the reduction of the recombination of photo-generated electron-hole pairs. Consequently, this TiO_2 based PSC exhibited a PCE of 13.42%, which was higher than that of the reference device using P25 as

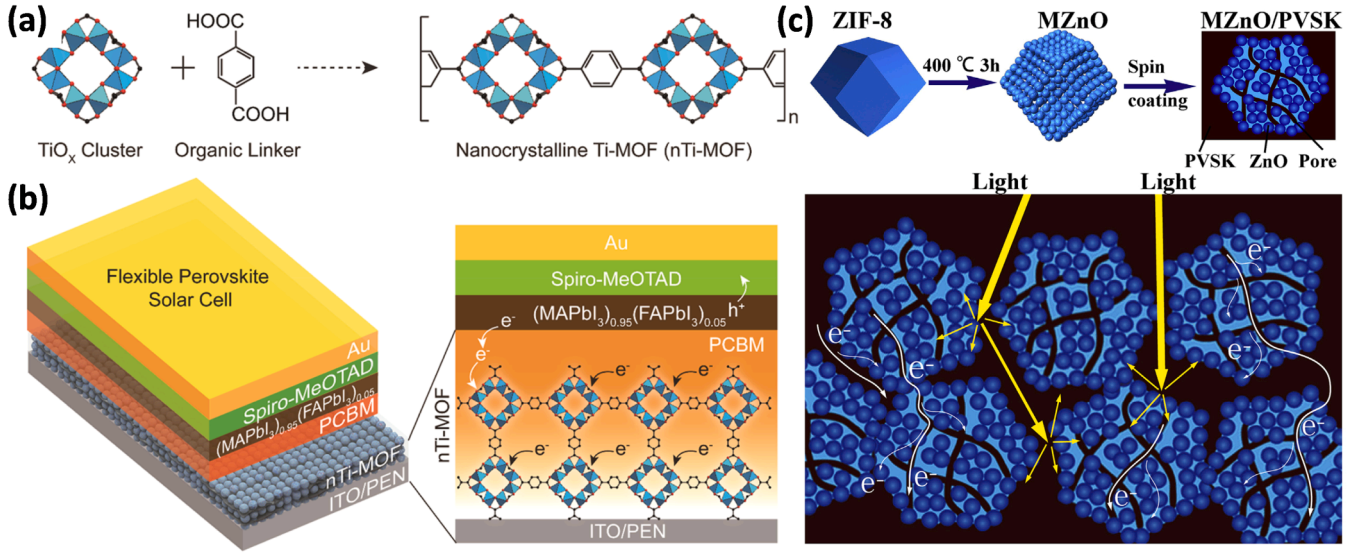

Fig. 8. Schematic illustration of (a) the synthesis process for MIL-125 (Ti) (nTi-MOF), which consists of linked TiO_2 clusters and BDC molecules, (b) the structure of nTi-MOF/PCBM ETL integrated PSC device, in which the magnified image shows the electron and hole transfer from the perovskite toward nTi-MOF/PCBM and spiro-MeOTAD, respectively. Reproduced with permission [211]. Copyright 2018, American Chemical Society. (c) The synthesis of ZIF-8 derived ZnO polyhedral as well as its use as ETL to improve light harvesting and electron extraction. Reproduced with permission [216]. Copyright 2020, Elsevier B. V.

ETL (i.e. 9.88%). In addition, the same group also synthesized mesoporous anatase TiO_2 nanocrystals from the pyrolysis of NH_2-MIL-125 (Ti) [88]. When using the screen-printing as-synthesized TiO_2 as an ETL, it was found that the ETL matched well with the conduction band of perovskite materials. It is worth noting that the screen-printing preparation method demonstrated by Liu et al. has a great potential to be a convenient process for commercial large-scale fabrication of carbon-based PSCs [87,88]. Fully printable PSC shows promise to achieve efficient and low-cost targets.

Moreover, there are also studies on the applications of ZIF-8 derivatives as ETL in PSCs [215,216]. Zhang et al. carbonized ZIF-8 thin films under a N_2 atmosphere to obtain porous carbon skeleton layers with good electrical conductivity [215]. The as-made porous carbon skeleton layer was deposited with TiO_2 nanoparticles and then used as the ETL to improve the photogenerated electron transport rate of PSCs. As a result, the PCE of the carbon-skeleton-based n-i-p PSC device was enhanced from 14.25% to 17.32% [215]. On the other hand, Yin et al. calcined ZIF-8 in air to obtain a ZnO electron extraction material [216]. The resulting polyhedral morphology and porous structure was used as ETL in the PSC. It increased the light adsorption capability and improved the interfacial contact with the perovskite layer, achieving a high PCE value of 18.1% (shown in Fig. 8c).

5.3. Utilization of MOFs and derivatives in hole transport layer for PSCs

The hole transport layer (HTL) enables hole extraction and transport in a PSC devices [218], as well as to prevent moisture or oxygen permeating into the perovskite layer, thus improving the stability of PSCs. Among the hole transport materials (HTM) for PSC, 2,2',7,7'-tetrakis-(N, N-dip-methoxyphenylamine) 9,9'-spirobifluorene (Spiro-OMeTAD) is the most widely used, mainly because of its high solubility and well-matched energy level [219,220]. However, it is still a challenge to improve the performance of Spiro-OMeTAD, due to its low conductivity, moderate hole mobility and low oxidation efficiency, which hinders the development of PSCs [220]. Compared to the limited number of studies on MOFs and derivatives in ETL, a greater amount of research has been carried out on the use of MOFs and their derivatives in HTLs for PSCs [221–228].

5.3.1. MOFs as HTL in PSCs

MOFs have recently attracted increasing attention in PSC applications due to their designable structures and controllable functionalities. However, the development of MOF-modified HTL for PSCs is still at an early stage. Yang et al. are the main research group focusing on the modification of HTL by the introduction of MOFs [221–224]. They first incorporated $[In_{0.5}K_{(3\text{-}qlc)}Cl_{1.5}(H_2O)_{0.5}]_{2n}$ (In10) into the HTL of the regular n-i-p PSC, to improve the oxidation capability of Spiro-OMeTAD [221]. It was found the incorporation of In10 could also increase the conductivity of HTL and improve the light response of PSCs, leading to an enhanced PCE over 20%. They then synthesized a hybrid polyoxometalate@MOF, $[Cu_2(BTC)_{4/3}\text{-}(H_2O)_2]_6[H_3PMo_{12}O_{40}]_2$ or POM@Cu-BTC, as a hybrid oxidant of HTL, using a simple self-assembly method [222]. The as-prepared POM@Cu-BTC could not only speed up the oxidation of Spiro-OMeTAD, but also improve the stability of the PSC device (n-i-p type). As a result, the as-fabricated PSC with the HTL containing POM@Cu-BTC achieved a high PCE value of 21.44%, with a long-term stability (i.e. 90% of the initial efficiency) under an ambient environment (Fig. 9a-d). Later, a highly stable MOF [Zn(Hcbob)]·(solvent)n, (Zn-CBOB)], was also prepared and used as a dopant for HTL in PSC [223]. Taking advantage of the conjugate frameworks and Lewis basic sites, the Zn-CBOB dopant could control the oxidation of Spiro-OMeTAD. Moreover, it could also coordinate with Pb^{2+}, passivating surface traps of the perovskite film. The Zn-CBOB doped PSC could achieve a PCE of 20.64%. Another study reported by Yang's group developed a thermally-stable In-based MOF $[In(HPyia)Cl_2]\cdot CH_3CN$, In-Pyia, to replace the volatile liquid-phase consisting of 4-tert-butylpyridine (t-BP) in HTL [224]. In-Pyia containing active pyridyl sites functioned as a morphological controller of HTL and a coordinator for Li^+ to prevent the negative morphological changes of HTL. The In-Pyia–based planar PSCs with a typical n-i-p configuration showed an improved PCE of 19.47 ± 0.79% with a low performance fluctuation, and enhanced the long-term stability under an ambient environment (i.e. maintaining 80.9% of the initial efficiency).

Moreover, Zeng et al. reported the synthesis of a 2D Pb-based MOF (Pb-MOF) with a hexagon sheet structure and evaluated its application as HTL when combined with Spiro-OMeTAD [225]. The oriented haloing effect of Pb-MOF was identified in the composite HTL, which led to a smooth and hydrophobic layer surface, as well as a good energy-level match with a perovskite/Ag layer. The PCE of the PSC (n-i-p type)

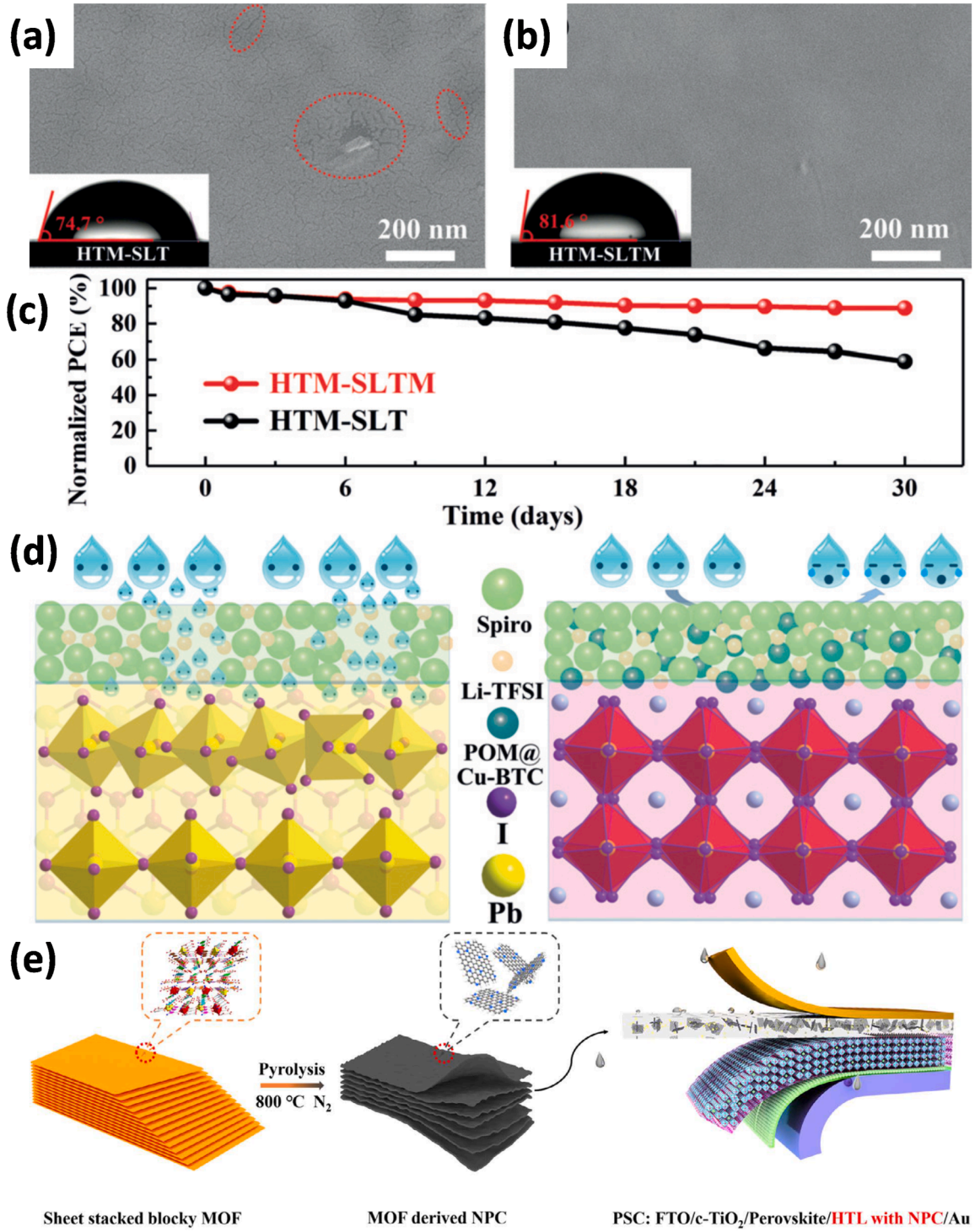

Fig. 9. (a-b) SEM images of different HTM-based PSC after a one-month long-term stability test. Reproduced with permission The red circles highlighted the cracks, and the insets illustrate the water contact angle of each HTL; (c) Long-term stability test - normalized PCE under different storage times; (d) Schematic illustration of enhanced stability mechanism for POM@Cu-BTC doped PSC. Reproduced with permission [222]. Copyright 2019, Wiley-VCH Verlag GmbH. (e) Schematic illustration of direct pyrolysis of 2D In-based MOF In-Aipa into NPC as an auxiliary additive for HTL in PSC. Reproduced with permission [227]. Copyright 2020, Wiley-VCH Verlag GmbH.

using composite HTL was 13.17%, which is 25% higher than that of the PSC using pure Spiro-OMeTAD.

In addition, Zhang et al. studied a MOF FJU-17 as an additive of the PSC HTL to improve stability of the PSC [226], and the In-based anionic framework FJU-17 acted as a capsule to contain $Me_2NH_2^+$ counter ions. Such a capsule incorporating the HTL could simultaneously provide defect passivation and hole mobility improvement of the as-fabricated n-i-p type PSC, which resulted in the average PCE improving by up to 19.50%. In addition, the as-fabricated PSC could maintain ~ 90% of the initial efficiency after running for 1000 h in air.

5.3.2. MOF derivatives as HTL in PSCs

The studies on the MOF derivatives as HTL in PSCs are currently limited. Yang et al. introduced a 2D graphitic N-rich porous carbon (NPC) into the HTL as an auxiliary additive [227], which was obtained from a direct carbonization of a 2D In-based MOF In-Aipa, [In_2(Hi-pa-NH_2)$_2$ (ipa-NH_2)$_2$]·5 H_2O, where H_2ipa·NH_2 is 5-aminoisophthalic acid (Fig. 9e). Due to the micro-meso-porous and hydrophobic nature of the NPC, the permeation of Li^+ and anode metals, as well as the moisture could be prevented. Thus, the PSC (n-i-p type) with NPC exhibited a high PCE of 18.51%, and a good long-term stability in air for over 720 h. In another example, Hazeghi et al. prepared core-shell CuO@NiO nanospheres by calcining bimetallic MOF Cu-Ni-BTC in air, and employed them as a p-type HTL for PSC [228]. The as-fabricated PSC PSC (n-i-p type) exhibited an enhanced PCE of 10.11%, which was mainly due to the good energy-level match of perovskite and HTL, and the decrease of defect density in the HTL. In addition, such an inorganic HTL-based PSC exhibited a longer stability than that of the PSC using Spiro-OMeTAD as the HTL.

5.4. Heterojunction perovskite/MOF layer in PSCs

The performance of PSCs can be severely affected by perovskite degradation induced due to the increasing surface defects and the imperfect grain boundaries of perovskite films. The incorporation of MOF into perovskite can not only modify the morphology and crystallinity of perovskite, but also reduce the defects and grain boundaries in the film obtained, further enhancing the performance of PSCs. In 2015, Ho et al. first incorporated Zr-based porphyrin MOF (MOF-525) nanocrystals as additives into the perovskite precursor solution, followed by a one-step deposition [229]. Three different MOF-525/perovskite precursor solution blending ratios were selected to study the effect of MOF-525 on the performance of PSCs. The PSC with planar n-i-p configuration using a perovskite film with ratio of 5 v/v% exhibited the optimal performance with the PCE of 12.0%. Moreover, two other types of stable Zr-based MOFs, UiO-66 and MOF-88, were investigated by Chueh et al. [85]. Both UiO-66 and MOF-88 modified NiO_x film could improve the UV-filtering capacity and perovskite crystallinity, thus the resulting modified p–i–n type PSCs exhibited a PCE of 17.01% and 16.55%, respectively. In addition, the perovskite/Zr-MOF hybrid (UiO-66/MOF-88) heterojunction films were also explored. As shown in Fig. 10a, both hybrid films exhibited a highly retarded degradation after the stability test, compared with the pristine film. It was found that such Zr-MOF hybrid showed a grain-locking effect. The Zr-MOF hybrid could not only passivate defects within the perovskite crystals, but also improve the film stability. This resulted in PCEs of 18.01% and 17.81% for the UiO-66-hybrid and MOF-88-hybrid PSCs, respectively (Fig. 10b). As shown in Fig. 10c, over 70% of the initial efficiency can remain during the long-term stability test (i.e. at 25 °C and under humidity of 60% for 2 weeks) [85].

In addition to Zr-based MOFs, Yang et al. synthesized microporous In-based MOF In-BTC nanocrystals by a facile method, which was incorporated as an additive into the perovskite to form a heterojunction light-harvesting layer [230]. They found that the microporous structure and terminal oxygen sites of In-BTC could not only improve the morphology/crystallinity, but also reduce the grain boundaries/defects of perovskite film. The perovskite/In-BTC heterojunction-based PSC with a typical n-i-p configuration exhibited an enhanced PCE of 19.63%, higher than that of the pristine PSC (18.19%). Moreover, the perovskite/In-BTC heterojunction-based PSC could retain over 80% of its initial efficiency after a 12-day long-term stability test under a high-humidity environment [230]. In addition, Fan et al. prepared formic acid-functionalized 2D MOF Zn-cbpp ([Zn(cbpp)(HCOO)]$_n$) as an agent for perovskite grain termination [231]. Due to the rich under-coordinated nitrogen atoms and functional carboxylate groups of Zn-cbpp, strong interactions including coordination bonds and hydrogen bonds could form between Zn-cbpp and perovskite (Fig. 10d), which resulted in the Zn-cbpp

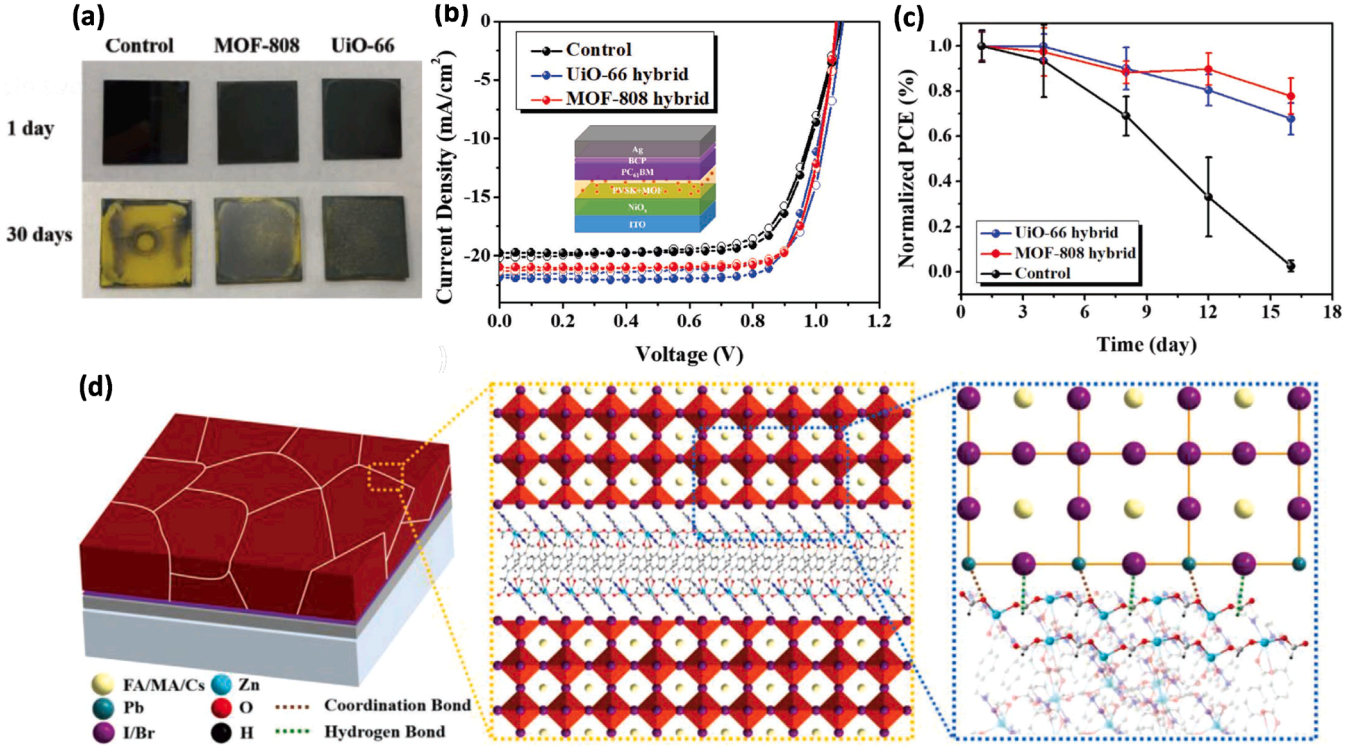

Fig. 10. (a) The real-time images of the Zr-MOF hybrid films and reference film stored under an ambient condition of 25 °C and relative humidity 60 ± 5%; (b) the J–V curves of the studied Zr-MOF-hybrid PSC and (c) the PCE of the fabricated devices stored in ambient condition of 25 °C and relative humidity 60 ± 5%. Reproduced with permission [85]. Copyright 2019, Wiley-VCH Verlag GmbH. (d) Schematic illustration of the perovskite/MOF heterojunction film modified with Zn-cbpp. Reproduced with permission [231]. Copyright 2021, Wiley-VCH Verlag GmbH.

modified perovskite films exhibiting enhanced optoelectronic properties and regular morphology with fewer defects. Consequently, the optimal Zn-cbpp-based PSC (n-i-p) exhibited a high PCE of 21.28%, with excellent moisture and thermal stabilities [231].

To explore the effect of different MOFs as additives within the perovskite layer on the PSC performance, four types of MOFs including Fe-terephthalate MOF (MOF-235), and MOFs consisting of Zr (IV), In (III) and Zn (II) with a LH_2 organic linker, were studied by Abedi et al. [232,233]. The effect of MOF weight percentage on the performance of its modified PSC was evaluated. It was found that the PCE of Zn-MOF-modified PSC was enhanced by more than 90% after the addition of 2 wt% of Zn-MOF into the perovskite layer. The stability of MOF-modified PSCs was also improved.

6. Applications in organic solar cells

To fulfil the requirement of materials in organic solar cells (OSCs), the photoactive organic semiconductive materials should simultaneously possess important requirements including: broad optical absorption (suitable bandgap), high absorption coefficient, good environmental stability, high charge mobility, thermal/light stability, proper solubility in different solvents and good film-forming capability [83]. MOFs and derivatives can meet some of the requirement in OSCs. Therefore, unlike the fast development of the applications of MOFs and derivatives in DSSCs and PSCs, MOFs and their derivatives have not been widely studied in OSCs. Only two relevant papers have been published so far [234,235]. Huang et al. first prepared a 2D tellurophene-based MOF for the inverted polymer OSC using tellurophene-2,5-dicarboxylate and cadmium nitrate [234]. Tellurophene is a unique constituent for organic semiconductors containing strong Te-Te interactions, which benefits interchain stacking and charge transport [236,237]. The as-synthesized MOF layers were then exfoliated by the polymer surfactant polyethylenimine ethoxylate (PEIE) to obtain nanosheet ink (MOF-PEIE ink) of single- or a few-layers (shown in Fig. 11a). The SEM and AFM image confirmed the belt-like morphology of MOF-PEIE with a nanosheet thickness of 1.3 nm (Fig. 11b-c). Such an ink was directly employed as an electron extraction layer (EEL) for OSCs, where its PCE value was enhanced in comparison with the PEIE-based OSC. However, the enhancement in the performance of the two MOF-PEIE ink-fabricated OSC devices was still very limited, with 7.88% in fullerene-based OSC and 4.84% in non-fullerene-based OSC devices [234].

Foster et al. explored the synthesis of ultrathin zinc-porphyrin-based MOF nanosheets, [Zn_2(ZnTCPP)], and then incorporated them into an active layer blend with polythiophene–fullerene (P3HT–PCBM) [235]. The optimized MOF-based OSC with hole only and electron only devices exhibited the highest performing PCE value of 5.2%, which is nearly double that of the reference OSC without using MOF (2.67%). A series of measurements suggest that the enhanced performance of MOF-based OSC devices is due to the presence of MOF nanosheets, which act as a template for the formation of P3HT crystals and as a barrier to inhibit the over-growth of PCBM (shown in Fig. 11d).

In summary, research indicates that 2D MOF nanosheets are promising potential nanomaterials for applications in OSCs, mainly because of their tuneable electronic and optical properties. They have potential to be blended with polymers such as non-fullerene acceptors to achieve high-performance in fullerene-free OSCs. In addition, the mechanism of the performance enhancement in MOF-based OSCs requires further investigation in the future.

7. Conclusions and outlooks

The recent progress on the applications of MOFs and MOF derivatives in different types of solar cells, namely DSSCs, PSCs and OSCs, has been discussed and analyzed in this review. MOFs possess unique structures with diverse tunability of their organic and inorganic components, which provide incredible chemical versatility. Depending on the photovoltaic and chemical properties of MOFs and MOF derivatives, they could be effectively utilized in solar cells as electrodes, photoactive materials and charge carriers.

Currently, the majority of studies are focused on the application of MOFs and MOF derivatives in DSSCs. When applied as a photoanode, MOFs can be used as either the active material, or the host for other active materials or the sensitizer. MOFs can also be used as an interfacial

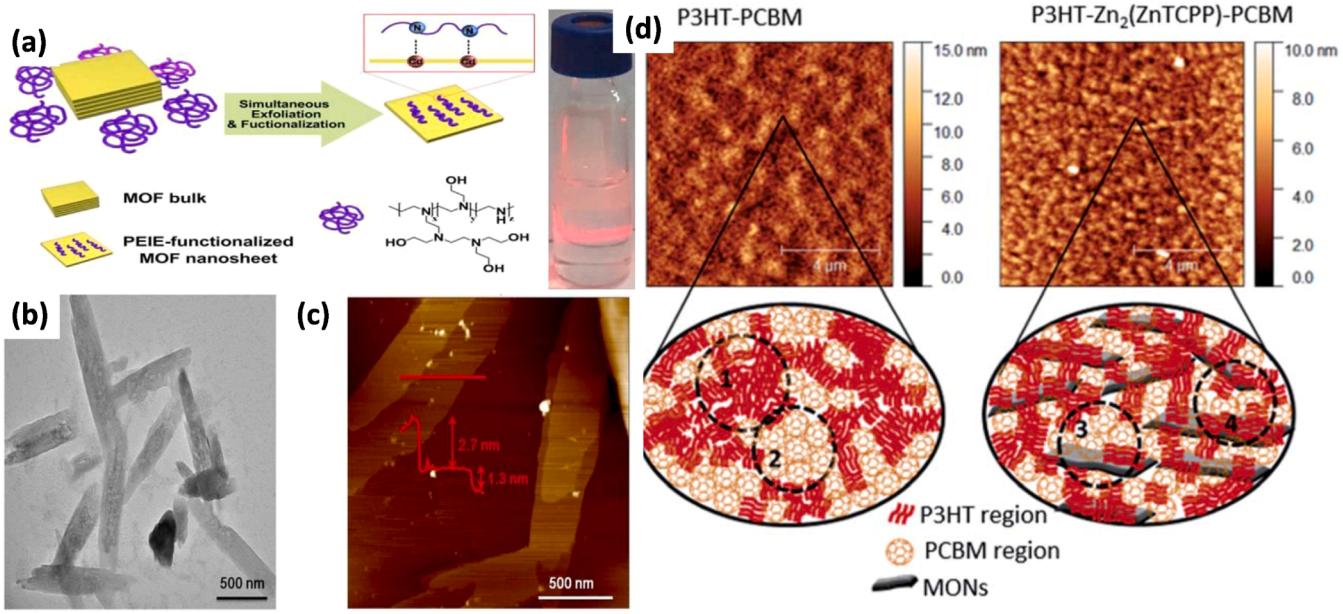

Fig. 11. (a) Schematic illustration of the process to synthesize 2D tellurophene-based MOF nanosheets through exfoliating and functionalizing with PEIE simultaneously; (b) TEM image of 2D tellurophene-based MOF-PEIE nanosheets; (c) AFM image of 2D tellurophene-based MOF-PEIE nanosheets, showing a thickness of 1.3 nm. Reproduced with permission [234]. Copyright 2018, Elsevier B.V. (d) AFM images of OSC devices following solvent and thermal annealing processes with (right) and without (left) Zn_2(ZnTCPP) nanosheets. The corresponding schematic illustration highlights that the nanosheets can promote the crystallinity of P3HT and prevent the over-growth of PCBM crystals. Reproduced with permission [235]. Copyright 2020, Royal Society of Chemistry.

modifier of the photoanode to improve the photovoltaic performance. Moreover, MOF derivatives in the form of metal oxides such as TiO_2 and ZnO are promising candidates as the photoanode. Generally, the direct use of MOF materials as photoanodes in DSSCs led to a low cell efficiency, this could be due to the sluggish charge transport in the electrically insulating MOF frameworks. Similarly, the electrically insulating characteristic of MOFs also limited their utilization as CE. It is more common for MOF derivatives to be applied as CE when compared to the pristine MOFs. It is worth noting that MOF derivatives including porous carbons, metal, metal sulfides, metal selenides, and metal carbides with various structures have been extensively studied. MOF derivative-based CEs can achieve a comparable or even higher cell efficiency than that of Pt, with great potential to replace the conventional Pt in DSSCs.

In terms of the applications of MOFs and MOF derivatives in PSCs, only limited studies have been reported so far. MOFs and MOF derivatives can be applied in various parts in PSC including interfacial layer, ETL, HTL, and heterojunction perovskite/MOF layer. They have been demonstrated to improve the quality/crystallinity of the perovskite film, enhance charge transfer, and inhibit the charge recombination, resulting in the enhancement of the power conversion efficiency and the cell stability of PSCs. Overall, the PCE and long-term stability have been improved due to the excellent thermal stability of MOFs. However, the working mechanisms behind these improvements are still not fully understood, more investigations are required to gain insight into the functions of relevant components, to build up the structure-performance relationship and provide theoretical guidance to further develop cost-effective MOF-based materials for PSC applications.

Although the emerging applications of MOFs and MOF derivatives in different types of solar cells have been developed rapidly and made encouraging advances in recent years, key challenges to improve the performance of solar cells are as follows:

(1) The low electron-conductivity of MOFs is one of the biggest obstacles for their application in solar cells. This could be improved by rational design and preparation of new types of MOFs. Functionalized MOFs with intrinsic electric conductive components or formation of MOFs-based composites with conductive materials could also provide solutions to increase the electronic conductivity of MOFs and their derivatives, enabling their applications in solar cells.
(2) The stability of solar cells, especially the stability of PSCs, is key to practical applications. Applications of MOFs and MOF derivatives in PSCs under conditions such as long term and high humidity should be regularly evaluated in future studies. It is important to develop PSCs with promising PCE and high stability performance which will pave concrete way to their potential practical applications.
(3) An in-depth understanding of the relationships between the structures, properties of MOFs/MOF derivatives and their photovoltaic performance are critically important. Elucidating the relationship between morphologies, topologies as well as dimensionality of different MOFs and derivatives with their PCE performance in solar cells will facilitate more promising MOF materials for solar cell applications. Further exploration of the applications of emerging 2-dimensional MOFs and their derivatives in solar cells may also bring about different new scenarios.
(4) Theoretical studies including simulation work and even the fast developed machine learning as well as AI technology are also very important tools to analyze the relevant parameters and properties of MOFs and MOF derivatives in solar cell applications. This will provide theoretical guidance on the further design and development of novel MOF-based materials for application in solar cells.

The increasing investigation of conductive MOF development, the further exploration of structures-performance relationships as well as the increasing understanding of the working mechanism of MOFs and MOF derivatives in solar cells, together with the effective support from theoretic studies, will exclusively inspire further design and development of novel MOFs and MOF derivatives for applications in different solar cells with enhanced performance in the near future.

Declaration of Competing Interest

The authors declare that they have no known competing financial interests or personal relationships that could have appeared to influence the work reported in this paper.

Data availability

Data will be made available on request.

Acknowledgements

This work was financially supported by the Leverhulme Trust (RPG-2018–320) and the Royal Society (IEC\NSFC\201121).

Declaration of Competing Interest

The authors declare no conflict of interest.

References

[1] M. Freitag, J. Teuscher, Y. Saygili, X. Zhang, F. Giordano, P. Liska, J. Hua, S. M. Zakeeruddin, J.E. Moser, M. Grätzel, A. Hagfeldt, Nat. Photonics 11 (2017) 372–378.
[2] Z. Sen, Solar Energy Fundamentals and Modeling Techniques: Atmosphere, Environment, Climate Change and Renewable Energy, Springer Science & Business Media,, 2008.
[3] B.R. Garrett, S.M. Polen, M. Pimplikar, C.M. Hadad, Y. Wu, J. Am. Chem. Soc. 139 (2017) 4342–4345.
[4] M. Grätzel, Philos. Trans. R. Soc. A 365 (2007) 993–1005.
[5] D.M. Chapin, C.S. Fuller, G.L. Pearson, J. Appl. Phys. 25 (1954) 676–677.
[6] A. Slade, Garboushian, V., 27.6% efficient silicon concentrator solar cells for mass production, In: Proceedings of the Technical Digest, 15th international photovoltaic science and engineering conference, Beijing, 2005.
[7] V. Bahrami-Yekta, T. Tiedje, Opt. Express 26 (2018) 28238–28248.
[8] M. Gorlatova, A. Wallwater, G. Zussman, Networking low-power energy harvesting devices: Measurements and algorithms, 2011 Proc. IEEE INFOCOM (2011) 1602–1610.
[9] A. Hagfeldt, G. Boschloo, L. Sun, L. Kloo, H. Pettersson, Chem. Rev. 110 (2010) 6595–6663.
[10] V. Sugathan, E. John, K. Sudhakar, Renew. Sustain. Energy Rev. 52 (2015) 54–64.
[11] J. Gong, K. Sumathy, Q. Qiao, Z. Zhou, Renew. Sustain. Energy Rev. 68 (2017) 234–246.
[12] G.D. Sharma, S.P. Singh, R. Kurchania, R.J. Ball, RSC Adv. 3 (2013) 6036–6043.
[13] M.A. Green, A. Ho-Baillie, H.J. Snaith, Nat. Photonics 8 (2014) 506–514.
[14] N.G. Park, Mater. Today 18 (2015) 65–72.
[15] M.I.H. Ansari, A. Qurashi, M.K. Nazeeruddin, J. Photochem. Photobiol., C. 35 (2018) 1–24.
[16] N. Kaur, M. Singh, D. Pathak, T. Wagner, J.M. Nunzi, Synth. Met. 190 (2014) 20–26.
[17] N. Yeh, P. Yeh, Renew. Sustain. Energy Rev. 21 (2013) 421–431.
[18] L. Duan, A. Uddin, Adv. Sci. 7 (2020) 1903259–1903297.
[19] H. Li, M. Eddaoudi, M. O'Keeffe, O.M. Yaghi, Nature 402 (1999) 276–279.
[20] O.M. Yaghi, M. O'Keeffe, N.W. Ockwig, H.K. Chae, M. Eddaoudi, J. Kim, Nature 423 (2003) 705–714.
[21] J.R.L. Hong-Cai Zhou, Omar M. Yaghi, Chem. Rev. 112 (2012) 673–674.
[22] J.L.C. Rowsell, O.M. Yaghi, Microporous Mesoporous Mater. 73 (2004) 3–14.
[23] M.P. Suh, H.J. Park, T.K. Prasad, D.W. Lim, Chem. Rev. 112 (2012) 782–835.
[24] J.R. Li, R.J. Kuppler, H.C. Zhou, Chem. Soc. Rev. 38 (2009) 1477–1504.
[25] P. Horcajada, R. Gref, T. Baati, P.K. Allan, G. Maurin, P. Couvreur, G. Férey, R. E. Morris, C. Serre, Chem. Rev. 112 (2012) 1232–1268.
[26] L. Wang, M. Zheng, Z. Xie, J. Mater. Chem. B 6 (2018) 707–717.
[27] A.H. Chughtai, N. Ahmad, H.A. Younus, A. Laypkov, F. Verpoort, Chem. Soc. Rev. 44 (2015) 6804–6849.
[28] J. Liu, L. Chen, H. Cui, J. Zhang, L. Zhang, C.Y. Su, Chem. Soc. Rev. 43 (2014) 6011–6061.
[29] Q. Wang, D. Astruc, Chem. Rev. 120 (2020) 1438–1511.
[30] S.N. Zhao, Y. Zhang, S.Y. Song, H.J. Zhang, Coord. Chem. Rev, 398, 2019, pp. 113007–113033.

[31] L.E. Kreno, K. Leong, O.K. Farha, M. Allendorf, R.P. Van Duyne, J.T. Hupp, Chem. Rev. 112 (2012) 1105–1125.
[32] H.Y. Li, S.N. Zhao, S.-Q. Zang, J. Li, Chem. Soc. Rev. 49 (2020) 6364–6401.
[33] Y.V. Kaneti, J. Tang, R.R. Salunkhe, X. Jiang, A. Yu, K.C.W. Wu, Y. Yamauchi, Adv. Mater. 29 (2017) 1604898–1604937.
[34] S. Dang, Q.L. Zhu, Q. Xu, Nat. Rev. Mater. 3 (2017) 17075–17088.
[35] M.Z. Hussain, Z. Yang, Z. Huang, Q. Jia, Y. Zhu, Y. Xia, Adv. Sci. 8 (2021) 2100625–2100654.
[36] H.B. Wu, X.W. Lou, Sci. Adv. 3 (2017) 9252–9267.
[37] M.Z. Hussain, B. van der Linden, Z. Yang, Q. Jia, H. Chang, R.A. Fischer, F. Kapteijn, Y. Zhu, Y. Xia, J. Mater. Chem. A 9 (2021) 4103–4116.
[38] C. Wang, J. Kim, J. Tang, M. Kim, H. Lim, V. Malgras, J. You, Q. Xu, J. Li, Y. Yamauchi, Chem 6 (2020) 19–40.
[39] Z. Huang, Z. Yang, M.Z. Hussain, Q. Jia, Y. Zhu, Y. Xia, J. Mater. Sci. Technol. 84 (2021) 76–85.
[40] M.Z. Hussain, Z. Yang, B. v.d. Linden, Z. Huang, Q. Jia, E. Cerrato, R.A. Fischer, F. Kapteijn, Y. Zhu, Y. Xia, J. Energy Chem. 57 (2021) 485–495.
[41] L.H. Xie, M.M. Xu, X.M. Liu, M.J. Zhao, J.R. Li, Adv. Sci. 7 (2020) 1901758–1901801.
[42] Z. Huang, Z. Yang, Q. Jia, N. Wang, Y. Zhu, Y. Xia, Nanoscale 14 (2022) 4726–4739.
[43] M.Z. Hussain, Z. Yang, A.M.E. Khalil, S. Hussain, S.U. Awan, Q. Jia, R.A. Fischer, Y. Zhu, Y. Xia, J. Mater. Sci. Technol. 101 (2022) 49–59.
[44] H. Wang, Q.L. Zhu, R. Zou, Q. Xu, Chem 2 (2017) 52–80.
[45] V. Stavila, A.A. Talin, M.D. Allendorf, Chem. Soc. Rev. 43 (2014) 5994–6010.
[46] M.D. Allendorf, A. Schwartzberg, V. Stavila, A.A. Talin, Chem. Eur. J. 17 (2011) 11372–11388.
[47] V. Bon, Curr. Opin. Green. Sustain. Chem. 4 (2017) 44–49.
[48] F.X. Llabrés i Xamena, A. Corma, H. Garcia, J. Phys. Chem. C. 111 (2007) 80–85.
[49] H.A. Lopez, A. Dhakshinamoorthy, B. Ferrer, P. Atienzar, M. Alvaro, H. Garcia, J. Phys. Chem. C. 115 (2011) 22200–22206.
[50] S. Goswami, L. Ma, A.B.F. Martinson, M.R. Wasielewski, O.K. Farha, J.T. Hupp, ACS Appl. Mater. Interfaces 8 (2016) 30863–30870.
[51] W.A. Maza, A.J. Haring, S.R. Ahrenholtz, C.C. Epley, S.Y. Lin, A.J. Morris, Chem. Sci. 7 (2016) 719–727.
[52] R. Khajavian, K. Ghani, J. Cryst. Growth 455 (2016) 60–65.
[53] E.D. Spoerke, L.J. Small, M.E. Foster, J. Wheeler, A.M. Ullman, V. Stavila, M. Rodriguez, M.D. Allendorf, J. Phys. Chem. C. 121 (2017) 4816–4824.
[54] C.C. Chueh, C.I. Chen, Y.A. Su, H. Konnerth, Y.J. Gu, C.W. Kung, K.C.W. Wu, J. Mater. Chem. A 7 (2019) 17079–17095.
[55] D.Y. Heo, H.H. Do, S.H. Ahn, S.Y. Kim, Polymers 12 (2020) 2061–2091.
[56] M.E. Hilal, A. Aboulouard, A.R. Akbar, H.A. Younus, N. Horzum, F. Verpoort, Catalysts 10 (2020) 897–927.
[57] R. Khajavian, M. Mirzaei, H. Alizadeh, Dalton Trans. 49 (2020) 13936–13947.
[58] X. Zhang, A. Chen, M. Zhong, Z. Zhang, X. Zhang, Z. Zhou, X.H. Bu, Electrochem. Energy Rev. 2 (2019) 29–104.
[59] R. Kaur, K.H. Kim, A.K. Paul, A. Deep, J. Mater. Chem. A 4 (2016) 3991–4002.
[60] O. Yildirim, M. Bonomo, N. Barbero, C. Atzori, B. Civalleri, F. Bonino, G. Viscardi, C. Barolo, Energies 13 (2020) 5602–5649.
[61] M. Shen, Y. Zhang, H. Xu, H. Ma, iScience 24 (2021) 103069–103096.
[62] W. Lu, Z. Wei, Z.Y. Gu, T.F. Liu, J. Park, J. Park, J. Tian, M. Zhang, Q. Zhang, T. Gentle Iii, M. Bosch, H.C. Zhou, Chem. Soc. Rev. 43 (2014) 5561–5593.
[63] S. Yuan, J.S. Qin, C.T. Lollar, H.C. Zhou, ACS Cent. Sci. 4 (2018) 440–450.
[64] C.P. Raptopoulou, Materials 14 (2021) 310–341.
[65] P. Wang, G. Wu, R. Wang, X. Wang, J. Inorg. Organomet. Polym. Mater. 22 (2012) 1028–1033.
[66] B.K. Tripuramallu, S. Mukherjee, S.K. Das, Cryst. Growth Des. 12 (2012) 5579–5597.
[67] S.A. Dalrymple, G.K.H. Shimizu, J. Am. Chem. Soc. 129 (2007) 12114–12116.
[68] M. Safaei, M.M. Foroughi, N. Ebrahimpoor, S. Jahani, A. Omidi, M. Khatami, TrAC, Trends Anal. Chem. 118 (2019) 401–425.
[69] Z. Ni, R.I. Masel, J. Am. Chem. Soc. 128 (2006) 12394–12395.
[70] R. Vakili, S. Xu, N. Al-Janabi, P. Gorgojo, S.M. Holmes, X. Fan, Microporous Mesoporous Mater. 260 (2018) 45–53.
[71] W.J. Son, J. Kim, J. Kim, W.S. Ahn, ChemComm (2008) 6336–6338.
[72] D.A. Yang, H.Y. Cho, J. Kim, S.T. Yang, W.S. Ahn, Energy Environ. Sci. 5 (2012) 6465–6473.
[73] N. Campagnol, T. Van Assche, T. Boudewijns, J. Denayer, K. Binnemans, D. De Vos, J. Fransaer, J. Mater. Chem. A 1 (2013) 5827–5830.
[74] H.M. Yang, X.L. Song, T.L. Yang, Z.H. Liang, C.M. Fan, X.G. Hao, RSC Adv. 4 (2014) 15720–15726.
[75] D. Lv, Y. Chen, Y. Li, R. Shi, H. Wu, X. Sun, J. Xiao, H. Xi, Q. Xia, Z. Li, J. Chem. Eng. Data 62 (2017) 2030–2036.
[76] Y. Chen, H. Wu, Z. Liu, X. Sun, Q. Xia, Z. Li, Ind. Eng. Chem. Res. 57 (2018) 703–709.
[77] I. Ahmed, S.H. Jhung, Mater. Today 17 (2014) 136–146.
[78] L. Feng, K.Y. Wang, J. Powell, H.C. Zhou, Matter 1 (2019) 801–824.
[79] W. Liu, R. Yin, X. Xu, L. Zhang, W. Shi, X. Cao, Adv. Sci. 6 (2019) 1802373–1802404.
[80] L. Jiao, H.L. Jiang, Chem 5 (2019) 786–804.
[81] P. Behera, S. Subudhi, S.P. Tripathy, K. Parida, Coord. Chem. Rev, 456, 2022, pp. 214392–214419.
[82] X. Bai, J. Liu, Q. Liu, R. Chen, X. Jing, B. Li, J. Wang, Eur. J. Chem. 23 (2017) 14839–14847.
[83] W. He, R. Ifraemov, A. Raslin, I. Hod, Adv. Funct. Mater. 28 (2018) 1707244–1707252.
[84] V. Chernikova, O. Shekhah, M. Eddaoudi, ACS Appl. Mater. 8 (2016) 20459–20464.
[85] C.C. Lee, C.I. Chen, Y.T. Liao, K.C.W. Wu, C.C. Chueh, Adv. Sci. 6 (2019) 1801715–1801723.
[86] D.Y. Lee, D.V. Shinde, S.J. Yoon, K.N. Cho, W. Lee, N.K. Shrestha, S.H. Han, J. Phys. Chem. 118C (2014) 16328–16334.
[87] X. Zhao, J. Zhao, J. He, B. Li, Y. Zhang, J. Hu, H. Wang, D. Zhang, Q. Liu, A.C. S. Appl, Energy Mater. 3 (2020) 6180–6187.
[88] B. Li, J. Zhao, Q. Lu, S. Zhou, H. Wei, T. Lv, Y. Zhang, J. Zhang, Q. Liu, Energy Technol. 9 (2021) 2000957–2000965.
[89] M. Seri, F. Mercuri, G. Ruani, Y. Feng, M. Li, Z.X. Xu, M. Muccini, Energy Technol. 9 (2021) 2000901–2000930.
[90] M.P. Paranthaman, W. Wong-Ng, R.N. Bhattacharya, Semiconductor Materials for Solar Photovoltaic Cells, Springer,, 2016.
[91] M.V. Dambhare, B. Butey, S.V. Moharil, J. Phys. Conf. Ser. 1913 (2021) 12053–12069.
[92] K.K.J. Shruti Sharma, Ashutosh Sharma, Mater. Sci. Appl. 6 (2015) 1145–1155.
[93] O. Vigil-Galán, M. Courel, J.A. Andrade-Arvizu, Y. Sánchez, M. Espíndola-Rodríguez, E. Saucedo, D. Seuret-Jiménez, M. Titsworth, J. Mater. Sci.: Mater. Electron. 26 (2015) 5562–5573.
[94] C.P. Muzzillo, Sol. Energy Mater. Sol. Cells 172 (2017) 18–24.
[95] J. Yan, B.R. Saunders, RSC Adv. 4 (2014) 43286–43314.
[96] G. Conibeer, Mater. Today 10 (2007) 42–50.
[97] S. Emin, S.P. Singh, L. Han, N. Satoh, A. Islam, Sol. Energy 85 (2011) 1264–1282.
[98] K. Ramasamy, M.A. Malik, P. O'Brien, Chem. Commun. 48 (2012) 5703–5714.
[99] M. Wu, X. Lin, Y. Wang, L. Wang, W. Guo, D. Qi, X. Peng, A. Hagfeldt, M. Grätzel, T. Ma, J. Am. Chem. Soc. 134 (2012) 3419–3428.
[100] J. Jiu, F. Wang, M. Sakamoto, J. Takao, M. Adachi, J. Electrochem. Soc. 151 (2004) A1653.
[101] Y. Ren, D. Zhang, J. Suo, Y. Cao, F.T. Eickemeyer, N. Vlachopoulos, S. M. Zakeeruddin, A. Hagfeldt, M. Grätzel, Nature (2022), https://doi.org/10.1038/s41586-022-05460-z.
[102] M. Grätzel, J. Photochem. Photobiol. C. 4 (2003) 145–153.
[103] M. Kim, J. Jeong, H. Lu, T.K. Lee, F.T. Eickemeyer, Y. Liu, I.W. Choi, S.J. Choi, Y. Jo, H.B. Kim, S.I. Mo, Y.K. Kim, H. Lee, N.G. An, S. Cho, W.R. Tress, S. M. Zakeeruddin, A. Hagfeldt, J.Y. Kim, M. Grätzel, D.S. Kim, Science 375 (2022) 302–306.
[104] S. Sun, T. Salim, N. Mathews, M. Duchamp, C. Boothroyd, G. Xing, T.C. Sum, Y. M. Lam, Energy Environ. Sci. 7 (2014) 399–407.
[105] NREL, 2022. ⟨https://www.nrel.gov/pv/cell-efficiency.html⟩.
[106] J.H. Park, J.Y. Kim, Matter 5 (2022) 3091–3093.
[107] Y. Cai, L. Huo, Y. Sun, Adv. Mater. 29 (2017) 1605437–1605474.
[108] G. Zhang, J. Zhao, P.C.Y. Chow, K. Jiang, J. Zhang, Z. Zhu, J. Zhang, F. Huang, H. Yan, Chem. Rev. 118 (2018) 3447–3507.
[109] J. Zhang, H.S. Tan, X. Guo, A. Facchetti, H. Yan, Nat. Energy 3 (2018) 720–731.
[110] S. Li, C.Z. Li, M. Shi, H. Chen, ACS Energy Lett. 5 (2020) 1554–1567.
[111] Q. Liu, Y. Jiang, K. Jin, J. Qin, J. Xu, W. Li, J. Xiong, J. Liu, Z. Xiao, K. Sun, S. Yang, X. Zhang, L. Ding, Sci. Bull. 65 (2020) 272–275.
[112] Y. Cui, Y. Xu, H. Yao, P. Bi, L. Hong, J. Zhang, Y. Zu, T. Zhang, J. Qin, J. Ren, Z. Chen, C. He, X. Hao, Z. Wei, J. Hou, Adv. Mater. 33 (2021) 2102420.
[113] L. Hong, H. Yao, Y. Cui, Z. Ge, J. Hou, APL Mater. 8 (2020) 120901–120911.
[114] Z. Song, S. Watthage, A. Phillips, M. Heben, J. Photonics Energy 6 (2016) 22001–220023.
[115] K. Sharma, V. Sharma, S.S. Sharma, Nanoscale Res. Lett. 13 (2018) 381–426.
[116] D.Y. Lee, C.Y. Shin, S.J. Yoon, H.Y. Lee, W. Lee, N.K. Shrestha, J.K. Lee, S.H. Han, Sci. Rep. 4 (2014) 3930–3934.
[117] D.Y. Lee, E.K. Kim, C.Y. Shin, D.V. Shinde, W. Lee, N.K. Shrestha, J.K. Lee, S. H. Han, RSC Adv. 4 (2014) 12037–12042.
[118] D.Y. Lee, I. Lim, C.Y. Shin, S.A. Patil, W. Lee, N.K. Shrestha, J.K. Lee, S.H. Han, J. Mater. Chem. A 3 (2015) 22669–22676.
[119] D.Y. Ahn, D.Y. Lee, C.Y. Shin, H.T. Bui, N.K. Shrestha, L. Giebeler, Y.Y. Noh, S. H. Han, ACS Appl. Mater. Interfaces 9 (2017) 12930–12935.
[120] J. Liu, W. Zhou, J. Liu, I. Howard, G. Kilibarda, S. Schlabach, D. Coupry, M. Addicoat, S. Yoneda, Y. Tsutsui, T. Sakurai, S. Seki, Z. Wang, P. Lindemann, E. Redel, T. Heine, C. Wöll, Angew. Chem. Int. Ed. 54 (2015) 7441–7445.
[121] J. Liu, W. Zhou, J. Liu, Y. Fujimori, T. Higashino, H. Imahori, X. Jiang, J. Zhao, T. Sakurai, Y. Hattori, W. Matsuda, S. Seki, S.K. Garlapati, S. Dasgupta, E. Redel, L. Sun, C. Wöll, J. Mater. Chem. A 4 (2016) 12739–12747.
[122] S. Ahmad, J. Liu, W. Ji, L. Sun, Materials 11 (2018) 1868–1875.
[123] M.A. Gordillo, D.K. Panda, S. Saha, ACS Appl. Mater. Interfaces 11 (2019) 3196–3206.
[124] X. Du, R. Fan, X. Wang, G. Yu, L. Qiang, P. Wang, S. Gao, Y. Yang, Cryst. Growth Des. 16 (2016) 1737–1745.
[125] R. Kaur, K.H. Kim, A. Deep, Appl. Surf. Sci. 396 (2017) 1303–1309.
[126] S. Alwin, V. Ramasubbu, X.S. Shajan, Bull. Mater. Sci. 41 (2018) 27–35.
[127] V. Ramasubbu, P.R. Kumar, E.M. Mothi, K. Karuppasamy, H.S. Kim, T. Maiyalagan, X.S. Shajan, Appl. Surf. Sci. 496 (2019) 143646–143656.
[128] P. Ram Kumar, V. Ramasubbu, X. Sahaya Shajan, E.M. Mothi, Mater. Today Energy 18 (2020) 100511–100517.
[129] W. Moloto, P. Mbule, E. Nxumalo, B. Ntsendwana, J. Photochem. Photobiol. A 407 (2021) 113063–113075.
[130] L.G. da Trindade, K.M.N. Borba, A.B. Trench, L. Zanchet, V. Teodoro, F.M. L. Pontes, E. Longo, T.M. Mazzo, J. Solid State Chem. 293 (2021) 121794–121817.

[131] A. Santiago Portillo, H.G. Baldoví, M.T. García Fernandez, S. Navalón, P. Atienzar, B. Ferrer, M. Alvaro, H. Garcia, Z. Li, J. Phys. Chem. C. 121 (2017) 7015–7024.
[132] Y. Li, A. Pang, C. Wang, M. Wei, J. Mater. Chem. 21 (2011) 17259–17264.
[133] Y. Li, C. Chen, X. Sun, J. Dou, M. Wei, ChemSusChem 7 (2014) 2469–2472.
[134] A. Gu, W. Xiang, T. Wang, S. Gu, X. Zhao, Sol. Energy 147 (2017) 126–132.
[135] Y. He, W. Wang, J. Solid State Chem. 296 (2021) 121992–121998.
[136] Y. He, Z. Zhang, W. Wang, L. Fu, J. Alloy. Compd. 825 (2020) 154089–154096.
[137] R. Khajavian, K. Ghani, J. Solid State Chem. 262 (2018) 94–99.
[138] J. Dou, Y. Li, F. Xie, X. Ding, M. Wei, Cryst. Growth Des. 16 (2016) 121–125.
[139] W.S. Chi, D.K. Roh, C.S. Lee, J.H. Kim, J. Mater. Chem. A 3 (2015) 21599–21608.
[140] J.T. Park, J. Moon, G.H. Choi, S.M. Lim, J.H. Kim, J. Ind. Eng. Chem. 84 (2020) 384–392.
[141] R. Tang, Z. Xie, S. Zhou, Y. Zhang, Z. Yuan, L. Zhang, L. Yin, ACS Appl. Mater. Interfaces 8 (2016) 22201–22212.
[142] R. Tang, R. Yin, S. Zhou, T. Ge, Z. Yuan, L. Zhang, L. Yin, J. Mater. Chem. A 5 (2017) 4962–4971.
[143] X. Zheng, W. Chen, L. Chen, Y. Wang, X. Guo, J. Wang, E. Wang, Chem. Eur. J. 23 (2017) 8871–8878.
[144] N.A. Kotov, J. Mater. Chem. 21 (2011) 16673–16674.
[145] Y.P. Gao, C.N. Sisk, L.J. Hope-Weeks, Chem. Mater. 19 (2007) 6007–6011.
[146] T. Kundu, S.C. Sahoo, R. Banerjee, Cryst. Growth Des. 12 (2012) 2572–2578.
[147] Y. Li, Z. Che, X. Sun, J. Dou, M. Wei, Chem. Commun. 50 (2014) 9769–9772.
[148] Q. Liu, Z.X. Low, Y. Feng, S. Leong, Z. Zhong, J. Yao, K. Hapgood, H. Wang, Microporous Mesoporous Mater. 194 (2014) 1–7.
[149] T. Enomoto, S. Ueno, E. Hosono, M. Hagiwara, S. Fujihara, CrystEngComm 19 (2017) 2844–2851.
[150] T.Y. Chen, Y.J. Huang, C.T. Li, C.W. Kung, R. Vittal, K.C. Ho, Nano Energy 32 (2017) 19–27.
[151] A.N. Yang, J.T. Lin, C.T. Li, ACS Appl. Mater. Interfaces 13 (2021) 8435–8444.
[152] A.S.A. Ahmed, W. Xiang, I. Saana Amiinu, X. Zhao, N. J. Chem. 42 (2018) 17303–17310.
[153] Y.B. Tian, Y.Y. Wang, S.M. Chen, Z.G. Gu, J. Zhang, ACS Appl. Mater. Interfaces 12 (2020) 1078–1083.
[154] F. Gong, H. Wang, X. Xu, G. Zhou, Z.S. Wang, J. Am. Chem. Soc. 134 (2012) 10953–10958.
[155] Z. Xie, X. Cui, W. Xu, Y. Wang, Electrochim. Acta 229 (2017) 361–370.
[156] F. Gong, X. Xu, Z. Li, G. Zhou, Z.S. Wang, Chem. Commun. 49 (2013) 1437–1439.
[157] Y. Xue, J. Liu, H. Chen, R. Wang, D. Li, J. Qu, L. Dai, Angew. Chem. Int. Ed. 51 (2012) 12124–12127.
[158] M. Wu, X. Lin, T. Wang, J. Qiu, T. Ma, Energy Environ. Sci. 4 (2011) 2308–2315.
[159] M. Wu, T. Ma, ChemSusChem 5 (2012) 1343–1357.
[160] T.N. Murakami, S. Ito, Q. Wang, M.K. Nazeeruddin, T. Bessho, I. Cesar, P. Liska, R. Humphry-Baker, P. Comte, P.T. Péchy, M. Grätzel, J. Electrochem. Soc. 153 (2006) A2255–A2261.
[161] S.H. Ahn, C.H. Lee, M.S. Kim, S.A. Kim, B. Kang, H.E. Kim, S.U. Lee, J.H. Bang, J. Phys. Chem. C. 121 (2017) 27332–27343.
[162] M.S. Wu, Y.C. Hou, J.C. Lin, J. Alloys, Compd 778 (2019) 662–668.
[163] J. Ou, C. Gong, J. Xiang, J. Liu, Sol. Energy 174 (2018) 225–230.
[164] H. Jing, X. Song, S. Ren, Y. Shi, Y. An, Y. Yang, M. Feng, S. Ma, C. Hao, Electrochim. Acta 213 (2016) 252–259.
[165] S.H. Hsu, C.T. Li, H.T. Chien, R.R. Salunkhe, N. Suzuki, Y. Yamauchi, K.C. Ho, K. C.W. Wu, Sci. Rep. 4 (2014) 6983–6988.
[166] X. Cui, Z. Xie, Y. Wang, Nanoscale 8 (2016) 11984–11992.
[167] X. Wang, Y. Xie, B. Bateer, K. Pan, X. Zhang, J. Wu, H. Fu, ACS Sustain. Chem. Eng. 7 (2019) 2784–2791.
[168] S.A. Liu, Z. Li, K. Zhao, M. Hao, Z. Zhang, L. Li, Y. Zhang, W. Zhang, J. Alloy. Compd. 831 (2020) 154910–154919.
[169] D. Tang, R. Zhao, J. Xie, K. Zhou, Y. Han, X. Wu, H. Wu, G. Diao, M. Chen, J. Alloy. Compd. 829 (2020) 154526–154533.
[170] X. Liu, X. Li, M. An, Y. Gao, Z. Cao, J. Liu, Electrochim. Acta 351 (2020) 136249–136259.
[171] C. Xu, J. Zhang, X. Qian, W. Wu, J. Yang, L. Hou, Electrochim. Acta 289 (2018) 448–458.
[172] X. Qian, W. Wu, J. Zhuang, Y. Niu, J. Huang, L. Hou, J. Power Sources 417 (2019) 21–28.
[173] J. Huang, X. Qian, J. Yang, Y. Niu, C. Xu, L. Hou, Electrochim. Acta 340 (2020) 135949–135959.
[174] W. Lu, R. Jiang, X. Yin, L. Wang, Nano Res 12 (2019) 159–163.
[175] Y. Li, X. Liu, H. Li, D. Shi, Q. Jiao, Y. Zhao, C. Feng, X. Bai, H. Wang, Q. Wu, J. Power Sources 422 (2019) 122–130.
[176] T. Wang, Y. Li, H. Li, D. Shi, Q. Jiao, Y. Zhao, P. Su, W. Wang, Q. Wu, ACS Omega 5 (2020) 26253–26261.
[177] J. Yang, Y. Niu, J. Huang, L. Liu, X. Qian, Electrochim. Acta 330 (2020) 135333–135342.
[178] H. Liu, X. Qian, Y. Niu, M. Chen, C. Xu, K.Y. Wong, Chem. Eng. J. 383 (2020) 123129–123140.
[179] S. Huang, S. Li, Q. He, H. An, L. Xiao, L. Hou, Appl. Surf. Sci. 476 (2019) 769–777.
[180] J.B. Joo, M. Dahl, N. Li, F. Zaera, Y. Yin, Energy Environ. Sci. 6 (2013) 2082–2092.
[181] A. Li, P. Zhang, X. Chang, W. Cai, T. Wang, J. Gong, Small 11 (2015) 1892–1899.
[182] X. Liu, J. Iocozzia, Y. Wang, X. Cui, Y. Chen, S. Zhao, Z. Li, Z. Lin, Energy Environ. Sci. 10 (2017) 402–434.
[183] X. Sun, Y. Li, J. Dou, D. Shen, M. Wei, J. Power, Sources 322 (2016) 93–98.
[184] J. Ou, C. Gong, M. Wang, J. Xiang, J. Liu, Electrochim. Acta 286 (2018) 212–218.
[185] J.S. Kang, J. Kang, D.Y. Chung, Y.J. Son, S. Kim, S. Kim, J. Kim, J. Jeong, M.J. Lee, H. Shin, S. Park, S.J. Yoo, M.J. Ko, J. Yoon, Y.E. Sung, J. Mater. Chem. A 6 (2018) 20170–20183.
[186] A.S.A. Ahmed, W. Xiang, I.S. Amiinu, Z. Li, R. Yu, X. Zhao, Sustain. Energy Fuels 3 (2019) 1976–1987.
[187] A.S.A. Ahmed, W. Xiang, Z. Li, I.S. Amiinu, X. Zhao, Electrochim. Acta 292 (2018) 276–284.
[188] A.S.A. Ahmed, W. Xiang, F. Shui, B. Li, H.H.A. Younes, I.S. Amiinu, X. Zhao, Sol. Energy 218 (2021) 117–128.
[189] Y. Zhao, B. Song, X. Cui, Y. Ren, W. Yue, Y. Wang, Mater. Lett. 250 (2019) 193–196.
[190] M.S. Kim, J.H. Bang, J. Phys. Chem. C. 122 (2018) 13267–13276.
[191] J. Wu, W. Pan, Y. Lin, J. Zhu, Q.S. Jiang, Y. Zhao, R. Ji, Y. Zhang, J. Mater. Sci.: Mater. Electron. 31 (2020) 12309–12316.
[192] M.S. Wu, C.Y. Chen, Y.R. Chen, H.C. Shih, Electrochim. Acta 215 (2016) 50–56.
[193] S.L. Jian, Y.J. Huang, M.H. Yeh, K.C. Ho, J. Mater. Chem. A 6 (2018) 5107–5118.
[194] X. Jiang, H. Li, S. Li, S. Huang, C. Zhu, L. Hou, Chem. Eng. J. 334 (2018) 419–431.
[195] J. Ou, J. Xiang, J. Liu, L. Sun, ACS Appl. Mater. Interfaces 11 (2019) 14862–14870.
[196] J. Ou, B. Hu, S. He, W. Wang, Y. Han, Sol. Energy 201 (2020) 693–700.
[197] L. Chen, W. Chen, E. Wang, J. Power Sources 380 (2018) 18–25.
[198] L.S. Xie, G. Skorupskii, M. Dincă, Chem. Rev. 120 (2020) 8536–8580.
[199] F. Bella, R. Bongiovanni, R.S. Kumar, M.A. Kulandainathan, A.M. Stephan, J. Mater. Chem. A 1 (2013) 9033–9036.
[200] S. Sarwar, M.S. Lee, S. Park, T.T. Dao, A. Ullah, S. Hong, C.H. Han, Thin Solid Films 704 (2020) 138024–138028.
[201] J. Fan, L. Li, H.S. Rao, Q.L. Yang, J. Zhang, H.Y. Chen, L. Chen, D.B. Kuang, C. Y. Su, J. Mater. Chem. A 2 (2014) 15406–15413.
[202] Y.J. Dong, H.S. Rao, Y. Cao, H.Y. Chen, D.B. Kuang, C.Y. Su, J. Power Sources 343 (2017) 148–155.
[203] J.R. Harwell, T.K. Baikie, I.D. Baikie, J.L. Payne, C. Ni, J.T.S. Irvine, G. A. Turnbull, I.D.W. Samuel, Phys. Chem. Chem. Phys. 18 (2016) 19738–19745.
[204] D. Shen, A. Pang, Y. Li, J. Dou, M. Wei, Chem. Commun. 54 (2018) 1253–1256.
[205] H.Y. Chung, C.H. Lin, S. Prabu, H.W. Wang, J. Chin. Chem. Soc. 65 (2018) 1476–1481.
[206] M.R. Ahmadian-Yazdi, N. Gholampour, M. Eslamian, ACS Appl. Energy Mater. 3 (2020) 3134–3143.
[207] C. Li, S. Guo, J. Chen, Z. Cheng, M. Zhu, J. Zhang, S. Xiang, Z. Zhang, Nanoscale Adv. 3 (2021) 3554–3562.
[208] S. Wu, Z. Li, M.-Q. Li, Y. Diao, F. Lin, T. Liu, J. Zhang, P. Tieu, W. Gao, F. Qi, X. Pan, Z. Xu, Z. Zhu, A.K.Y. Jen, Nat. Nanotechnol. 15 (2020) 934–940.
[209] J. Dou, C. Zhu, H. Wang, Y. Han, S. Ma, X. Niu, N. Li, C. Shi, Z. Qiu, H. Zhou, Y. Bai, Q. Chen, Adv. Mater. 33 (2021) 2102947–2102955.
[210] T.M. Huyen Nguyen, C.W. Bark, J. Alloy. Compd. 841 (2020) 155711–155718.
[211] U. Ryu, S. Jee, J.S. Park, I.K. Han, J.H. Lee, M. Park, K.M. Choi, ACS Nano 12 (2018) 4968–4975.
[212] V.A. Gómez Andrade, W.O. Herrera Martínez, F. Redondo, N.B. Correa Guerrero, F. Roncaroli, M.D. Perez, Appl. Mater. Today 22 (2021) 100915–100923.
[213] X. Hou, L. Pan, S. Huang, O.Y. Wei, X. Chen, Electrochim. Acta 236 (2017) 351–358.
[214] T.M.H. Nguyen, C.W. Bark, ACS Omega 5 (2020) 2280–2286.
[215] Z. Zhang, X. Luo, B. Wang, J. Zhang, ACS Appl. Energy Mater. 2 (2019) 2760–2768.
[216] Y.N. Zhang, B. Li, L. Fu, Q. Li, L.W. Yin, Electrochim. Acta 330 (2020) 135280–135287.
[217] K.M. Choi, H.M. Jeong, J.H. Park, Y.B. Zhang, J.K. Kang, O.M. Yaghi, ACS Nano 8 (2014) 7451–7457.
[218] X. Zheng, H. Lei, G. Yang, W. Ke, Z. Chen, C. Chen, J. Ma, Q. Guo, F. Yao, Q. Zhang, H. Xu, G. Fang, Nano Energy 38 (2017) 1–11.
[219] Z. Hawash, L.K. Ono, S.R. Raga, M.V. Lee, Y. Qi, Chem. Mater. 27 (2015) 562–569.
[220] Z. Li, J. Tinkham, P. Schulz, M. Yang, D.H. Kim, J. Berry, A. Sellinger, K. Zhu, Adv. Energy Mater. 7 (2017) 1601451–1601458.
[221] M. Li, J. Wang, A. Jiang, D. Xia, X. Du, Y. Dong, P. Wang, R. Fan, Y. Yang, Sol. Energy 188 (2019) 380–385.
[222] Y. Dong, J. Zhang, Y. Yang, L. Qiu, D. Xia, K. Lin, J. Wang, X. Fan, R. Fan, Angew. Chem. Int. Ed. 58 (2019) 17610–17615.
[223] J. Wang, J. Zhang, Y. Yang, S. Gai, Y. Dong, L. Qiu, D. Xia, X. Fan, W. Wang, B. Hu, W. Cao, R. Fan, ACS Appl. Mater. Interfaces 13 (2021) 5235–5244.
[224] X. Zhou, L. Qiu, R. Fan, H. Ye, C. Tian, S. Hao, Y. Yang, J. Power Sources 473 (2020) 228556–228564.
[225] L. Huang, X. Zhou, R. Wu, C. Shi, R. Xue, J. Zou, C. Xu, J. Zhao, W. Zeng, J. Power Sources 433 (2019) 226699–226706.
[226] J. Zhang, S. Guo, M. Zhu, C. Li, J. Chen, L. Liu, S. Xiang, Z. Zhang, Chem. Eng. J. 408 (2021) 127328–127334.
[227] X. Zhou, L. Qiu, R. Fan, A. Wang, H. Ye, C. Tian, S. Hao, Y. Yang, Sol. RRL 4 (2020) 1900380–1900385.
[228] F. Hazeghi, S. Mozaffari, S.M.B. Ghorashi, J. Solid State Chem. 24 (2020) 1427–1438.
[229] T.H. Chang, C.W. Kung, H.W. Chen, T.Y. Huang, S.Y. Kao, H.C. Lu, M.H. Lee, K. M. Boopathi, C.W. Chu, K.C. Ho, Adv. Mater. 27 (2015) 7229–7235.
[230] X. Zhou, L. Qiu, R. Fan, J. Zhang, S. Hao, Y. Yang, Nano-Micro Lett. 12 (2020) 80–90.
[231] L. Qiu, K. Xing, J. Zhang, Y. Yang, W. Cao, X. Zhou, K. Zhu, D. Xia, R. Fan, Adv. Funct. Mater. 31 (2021) 2010368–2010378.

[232] M.S. Sowmehsaraee, M. Abedi, M. Ranjbar, J. Mater. Sci.: Mater. Electron. 32 (2021) 15143–15150.
[233] M. Seifpanah Sowmehesaraee, M. Ranjbar, M. Abedi, S.A. Mozaffari, Sol. Energy 214 (2021) 138–148.
[234] W. Xing, P. Ye, J. Lu, X. Wu, Y. Chen, T. Zhu, A. Peng, H. Huang, J. Power Sources 401 (2018) 13–19.
[235] K. Sasitharan, D.G. Bossanyi, N. Vaenas, A.J. Parnell, J. Clark, A. Iraqi, D. G. Lidzey, J.A. Foster, J. Mater. Chem. A 8 (2020) 6067–6075.
[236] R.S. Ashraf, I. Meager, M. Nikolka, M. Kirkus, M. Planells, B.C. Schroeder, S. Holliday, M. Hurhangee, C.B. Nielsen, H. Sirringhaus, I. McCulloch, J. Am. Chem. Soc. 137 (2015) 1314–1321.
[237] L. Yang, W. Gu, L. Lv, Y. Chen, Y. Yang, P. Ye, J. Wu, L. Hong, A. Peng, H. Huang, Angew. Chem. Int. Ed. 57 (2018) 1096–1102.

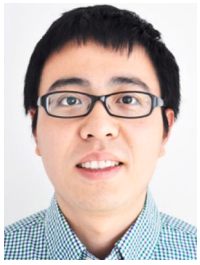

Dr Binling Chen completed his PhD in Materials Engineering from the University of Exeter. Since then, he has more than 6 years of research experience at the University of Exeter, the University of Bath, and Beijing Institute of Technology. His current research mainly focuses on advanced manufacturing, especially additive manufacturing (3D printing), of functional materials such as MOFs, their derivatives and other composites for energy and environment related applications. He has published more than 40 papers in international journals.

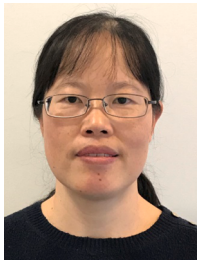

Zhuxian Yang received her BSc from East China Normal University in 1995 and her MSc from Fudan University, China in 1998. She earned her PhD in 2007 from the School of Chemistry at the University of Nottingham in the United Kingdom, working on the synthesis, characterization and application of micro/mesoporous carbon materials. She is now a Research Fellow in the College of Engineering, Mathematics and Physics Sciences, University of Exeter, working on the conversion of carbon dioxide to dimethyl carbonate. Her research interests include applications of porous materials in gas storage and separation, as catalysts and electrocatalysts.

Quanli Jia received his B.E. degree in non-organic materials from Hunan University in 1994 and received his M.S., and Ph. D. degree in Materials Science from Zhengzhou University, in 2004 and 2010, respectively. In 1994, he became an engineer in Zhengzhou White Dove Co. Ltd., since 2004, he became a lecturer, associate professor, professor at High Temperature Ceramics Institute, Zhengzhou University. His research interests are high performance castables, oxide-nonoxide refractory composites, low-dimensional nanomaterials and high temperature ceramics. He has co-authored more than 100 papers and authorized 10 patents.

Dr Richard Ball is a Reader in the Department of Architecture and Civil Engineering at the University of Bath. He is a Materials Scientist, Chartered Scientist, Chartered Engineer and Fellow of the Institute of Materials, Minerals and Mining. His research interests are focused on microstructure/ macrostructure property relationships of materials, setting reactions, sensors, degradation processes, water transport mechanisms, polymeric and ceramic materials for 3D printing, conservation materials, photocatalytic coatings, and materials for improving the indoor air quality of buildings. He is the author of 101 publications.

Yanqiu Zhu is a Chair of Functional Materials at University of Exeter since 2010. He obtained his BSc, MSc and PhD in China, in 1989, 1992 and 1996 respectively. He has research experience in China, Japan and the UK. He worked at University of Sussex and University of Nottingham, prior to joining Exeter. His research covers a wide range of materials science and engineering, with special interest in functional nanomaterials and nanocomposites. He is an author/co-author of over 200 journal publications.

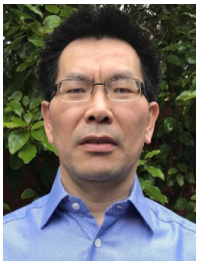

Yongde Xia earned his PhD from Fudan University, China. After postdoctoral experience in Korea and France, he moved to UK and worked as a Research Fellow at the University of Nottingham. Followed by joining Exeter in 2010, he is now a Senior Lecturer in Functional Materials in the College of Engineering, Mathematics and Physics Sciences at University of Exeter. His main research interests include novel porous materials for energy, electrochemical energy storage and conversion, photocatalysis and adsorption. He contributes to over 160 peer-reviewed journal publications.